DESIGN, MODELLING AND ANALYSIS OF MORPHING AIRFOILS

A THESIS SUBMITTED TO
THE GRADUATE SCHOOL OF NATURAL AND APPLIED SCIENCES
OF
MIDDLE EAST TECHNICAL UNIVERSITY

BY

BUĞRA KÖKSAL

IN PARTIAL FULFILLMENT OF THE REQUIREMENTS
FOR
THE DEGREE OF MASTER OF SCIENCE
IN
AEROSPACE ENGINEERING

JANUARY 2023

Approval of the thesis:

DESIGN, MODELLING AND ANALYSIS OF MORPHING AIRFOILS

submitted by **BUĞRA KÖKSAL** in partial fulfillment of the requirements for the degree of **Master of Science** i**n Aerospace Engineering, Middle East Technical University** by,

Prof. Dr. Halil Kalıpçılar
Dean, Graduate School of **Natural and Applied Sciences** _____

Prof. Dr. Serkan Özgen
Head of the Department, **Aerospace Engineering** _____

Assoc. Prof. Dr. Melin Şahin
Supervisor, **Aerospace Engineering, METU** _____

Prof. Dr. Oğuz Uzol
Co-Supervisor, **Aerospace Engineering, METU** _____

Examining Committee Members:

Prof. Dr. Serkan Özgen
Aerospace Engineering, METU _____

Assoc. Prof. Dr. Melin Şahin
Aerospace Engineering, METU _____

Prof. Dr. Oğuz Uzol
Aerospace Engineering, METU _____

Assoc. Prof. Dr. Ercan Gürses
Aerospace Engineering, METU _____

Asst. Prof. Dr. Onur Baş
Mechanical Engineering, TED University _____

Date: 27.01.2023

I hereby declare that all information in this document has been obtained and presented in accordance with academic rules and ethical conduct. I also declare that, as required by these rules and conduct, I have fully cited and referenced all material and results that are not original to this work.

Name Last name :

Signature :

ABSTRACT

DESIGN, MODELLING AND ANALYSIS OF MORPHING AIRFOILS

Köksal, Buğra
Master of Science, Aerospace Engineering
Supervisor: Assoc. Prof. Dr Melin Şahin
Co-Supervisor: Prof. Dr. Oğuz Uzol

January 2023, 67 pages

This study presents the design, finite element (FE) modeling and analysis of a morphing airfoil using pressure-actuated cell structures. It is aimed that the selected baseline airfoil should be capable of changing its profile to morph into a target airfoil profile. To achieve this goal, first, a NACA 0012 airfoil with a 500 mm chord and 8 mm x 8 mm outer cross-section is obtained in Altair® HyperWorks environment as a baseline airfoil. Following this, the cell actuators responsible for morphing are designed and located on this baseline airfoil. Here, cells with 8 mm x 8 mm cross-sections and a 1 mm thick elastomeric layer are used. Then, 1 mm thick and 2.4 mm spaced stiffening rings are incorporated into the cell actuator design. In total, ten cell actuators are placed; four on the upper and lower sides and two on the spars at 25% and 50% of the chord locations of the selected baseline airfoil.

Having completed the design phase, a finite element model is then created via Altair® HyperWorks comprising three-dimensional second-order elements. For the cell actuators, the neo-Hookean hyperelastic and isotropic material models are used to model elastomeric chambers and stiffening rings, respectively. The isotropic material is also assigned to the rest of the baseline airfoil.

Then, a targeting algorithm aiming to calculate the required pressure distribution inside the cell actuators is developed. It calculates them in such a way that the distance between selected morphed airfoil nodes and corresponding target airfoil points is minimized using a linear combination of the effects of each cell actuator located on the airfoil.

NACA 2412 airfoil is chosen as the target airfoil and via the targeting algorithm, the pressure distributions responsible for morphing are then calculated. In the end, these pressure distributions are applied to the baseline airfoil and both linear and non-linear finite element analyses are performed and the results are presented in the form of morphed structures.

The present study shows that with the help of a targeting algorithm, the required pressure distribution of cell actuators can be calculated and a morphing airfoil design comprising pressure-actuated cell structures is achievable with feasible pressure values.

Keywords: Morphing Structures, Airfoils, Pressurized Cells, Finite Element Modelling and Analysis

ÖZ

ŞEKİL DEĞİŞTİREN KANAT PROFİLLERİNİN TASARIM, MODELLEME VE ANALİZLERİ

Köksal, Buğra
Yüksek Lisans, Havacılık ve Uzay Mühendisliği
Tez Yöneticisi: Assoc. Dr. Melin Şahin
Ortak Tez Yöneticisi: Prof. Dr. Oğuz Uzol

Ocak 2023, 67 sayfa

Bu çalışma, basınç tahriki ile çalıştırılan hücre yapılarını kullanarak şekil değiştiren bir kanat profilinin tasarımını, sonlu eleman modellemesini ve analizini sunmaktadır. Seçilen temel kanat profilinin, hedef kanat profiline şekil değiştirebilmesi amaçlanmaktadır. Bu amaca ulaşmak için öncelikle Altair® HyperWorks ortamında temel kanat profili olarak 500 mm kirişli ve 8 mm x 8 mm dış kesitli bir NACA 0012 kanat profili çizilmiştir. Bunu takiben, şekil değiştirmeden sorumlu hücre aktüatörleri tasarlanmış ve bu temel kanat profiline yerleştirilmiştir. Burada 8 mm x 8 mm kesitli hücreler ve 1 mm kalınlığında elastomerik tabaka kullanılmıştır. Daha sonra hücre aktüatörü tasarımına 1 mm kalınlığında ve 2.4 mm aralıklı takviye halkalar dahil edilmiştir. Seçilen temel kanat profilinin üst ve alt kenarlarda dört, kiriş uzunluğunun %25'inde ve %50'sindeki direklerde iki, toplamda on hücre aktüatörü yerleştirilmiştir.

Tasarım aşaması tamamlandıktan sonra Altair® HyperWorks aracılığıyla üç boyutlu ikinci dereceden elemanlardan oluşan bir sonlu eleman modeli oluşturulmuştur. Hücre aktüatörleri için, sırasıyla, elastomerik odaları ve takviye halkalarını modellemek için Neo-Hookean hiperelastik ve izotropik malzeme modelleri kullanılmıştır. İzotropik malzeme ayrıca temel kanat profilinin geri kalanında da kullanılmıştır.

Ardından, hücre aktüatörler içindeki gerekli basınç dağılımını hesaplamayı amaçlayan bir hedefleme algoritması geliştirilmiştir. Bunlar, şekil değiştirmiş kanat profillerindeki seçilen noktalar ve hedef kanat profilindeki ilgili noktalar arasındaki mesafeyi en aza indirecek şekilde her bir hücre aktüatörünün ana yapıya etkisinin doğrusal kombinasyonu kullanılarak hesaplanmaktadır.

NACA 2412 kanat profili, hedef kanat profili olarak seçilmiştir ve hedefleme algoritması aracılığıyla, şekil değiştirmeden sorumlu basınç dağılımları hesaplanmıştır. Son olarak, bu basınç dağılımları kanat profiline uygulanmış ve hem doğrusal hem de doğrusal olmayan sonlu eleman analizleri yapılmış ve sonuçlar şekil değiştirmiş yapılar şeklinde sunulmuştur.

Mevcut çalışma, hedefleme algoritması yardımıyla hücre aktüatörlerinin gerekli basınç dağılımları hesaplanabilmekte ve basınç tahriki ile çalışan hücre yapılarını kullanan şekil değiştiren bir kanat profili tasarımının uygun basınç değerleri ile elde edilebileceğini de göstermektedir.

Anahtar Kelimeler: Şekil Değiştiren Yapılar, Kanat Profilleri, Basınç Tahrikli Hücreler, Sonlu Eleman Modelleme ve Analizleri

To all my loved ones

ACKNOWLEDGMENTS

First, I would like to express my gratitude to my supervisor Assoc. Prof. Dr. Melin Şahin for giving me an opportunity to work with him, allowing me to benefit from his invaluable comments and experiences and his support in completing my study.

Also, I would like to express my gratitude to my co-supervisor Prof. Dr. Oğuz Uzol for his support and contribution to my study.

I would like to express my special thanks to my mentors and chef engineers from TAI, Özkan Murat and Hande Işın Özdemir for the information they gave me on the Finite Element Method and Stress Engineering topics. Also, thanks for their support during my master's period.

Finally, special thanks and deepest gratitude to all my friends for their endless support.

TABLE OF CONTENTS

ABSTRACT iii

ÖZ v

ACKNOWLEDGMENTS viii

TABLE OF CONTENTS ix

LIST Of TABLES xi

LIST OF FIGURES xii

CHAPTER 1 1

1 INTRODUCTION 1

1.1 Background of the Study 2

1.2 Motivation and Objective of the Study 9

1.3 Outline of the Study 10

CHAPTER 2 13

2 DESIGN OF MORPHING AIRFOILS 13

2.1 Introduction 13

2.2 Baseline Airfoil Selection for the Morphing Application 13

2.3 Fluid Actuated Cell Design for the Morphing Airfoil 16

2.4 Material Selection of the Morphing Airfoil 19

2.5 Placement of the Cell Actuators 19

2.6 Conclusions 21

CHAPTER 3 23

3 UNIT LOAD METHOD AND TARGETING ALGORITHM 23

3.1 Introduction 23

3.2 Details of Finite Element Modelling 23

3.3 Linear Static Finite Element Analysis of Designed Airfoil with Unit Loads 25
3.4 Targeting Algorithm 26
3.5 Conclusion 32
CHAPTER 4 33
4 FINITE ELEMENT ANALYSIS OF THE MORPHING AIRFOIL 33
4.1 Introduction 33
4.2 Geometric Linear Static Finite Element Analysis of Designed Airfoil Using Calculated Load Combination 33
4.3 Geometric Non-Linear Static Finite Element Analysis of Designed Airfoil Using Calculated Load Combination 44
4.4 Conclusion 54
CHAPTER 5 57
5 CONCLUSION 57
5.1 General Conclusions 57
5.2 Recommendation for Future Work 58
REFERENCES 59
APPENDICES 59
APPENDIX A 63
APPENDIX B 66

LIST OF TABLES

TABLES

Table 3.1 Undeformed and Deformed X Coordinates of Selected Nodes 27
Table 3.2 Undeformed and Deformed Y Coordinates of Selected Nodes 28
Table 3.3 X displacements of Unit Load Cases 29
Table 3.4 Y displacements of Unit Load Cases 29
Table 3.5 Output of the Targeting Algorithm 32
Table 4.1 Pressure Distribution of the FE Model 35
Table 4.2 Targeting Algorithm- Linear FE Morphed Airfoil Result Comparison.. 36
Table 4.3 Strain and Stress Results of Actuators 42
Table 4.4 Modified Pressure Distribution 46
Table 4.5 Strain and Stress Results of Actuators 52
Table 4.6 Linear and Non-Linear Model Strain Comparison 55
Table 4.7 Linear and Non-Linear Model Stress Comparison 56

LIST OF FIGURES

FIGURES

Figure 1.1. Sweep Angle Change of a Bird [1] 2
Figure 1.2. Categorization of Morphing Types [2] 3
Figure 1.3. Morphing with Scissor-Structural Mechanism [3] 4
Figure 1.4. Servo Actuated Control Surface [5] 4
Figure 1.5. Capability of Servo Actuated Control Surface [5] 5
Figure 1.6. A Morphing Trailing Edge Design Using Pressurized Cell Structures [8] 6
Figure 1.7. Deformation of FAMoUS specimen [14] 6
Figure 1.8. Morphing Trailing Edge Design Using FAMoUS [13] 7
Figure 1.9. Deformation Plot of Finite Element Result of Designed Trailing Edge [13] 8
Figure 1.10. Deformation of 3D Printed Trailing Edge Specimen [11] 8
Figure 1.11. 3D Winglet Specimen Built Using Pressurized Cell Structures [11] 9
Figure 2.1. Main Geometric Parameters of an Aerodynamic Airfoil [18] 14
Figure 2.2. The Morphing Airfoil Without Cell Structures 15
Figure 2.3. Spar Locations of the Morphing Airfoil 15
Figure 2.4. Simple Prismatic Cell Design [11] 16
Figure 2.5. Force and Stoke Generation of the FAMoUS Concept [11] 17
Figure 2.6. Dimensions of the Cell Actuator for Designed Morphing Airfoil 18
Figure 2.7. Upper and Lower Cell Actuator Locations 20
Figure 2.8. Naming of the Cell Actuators 20
Figure 3.1. Mesh Image of Up1 Cell Actuator 24
Figure 3.2. Constraints Locations 25
Figure 3.3. Unit Load Case for Up1 Actuator 26
Figure 3.4. Selected Nodes (yellow) 27
Figure 4.1. Finite Element Model of Designed Airfoil 34
Figure 4.2. Loads and Boundary Conditions 34

Figure 4.3. Linear FE Analysis Deformation of the Designed Airfoil 37
Figure 4.4. Deformation at the Leading Edge Region 37
Figure 4.5. Deformation at the Middle Region 38
Figure 4.6. Deformation at the Trailing Edge Region 39
Figure 4.7. Von-Mises Strain Result of Elastomeric Chamber of Cell Actuators.. 40
Figure 4.8. Von-Mises Strain Result of Elastomeric Chamber of Up2 Actuators.. 40
Figure 4.9. Von-Mises Stress Result of Aluminum Region of the Morphing Airfoil. 41
Figure 4.10. Von-Mises Stress Result of Aluminum Stiffener of Up2 Actuator.... 41
Figure 4.11. Von-Mises Stress Result of Aluminum Stiffener of Up2 Actuator (Filtered) 42
Figure 4.12. Von-Mises Stress Result of Region where no Actuators are placed .. 43
Figure 4.13. Non-linear FE Result at Load Level 0 % and 100 % 44
Figure 4.14. Non-linear FE Result at Load Level 70.9 % and 82.4 % 45
Figure 4.15. Non-Linear FE Analysis Deformation of the Designed Airfoil 47
Figure 4.16. Deformation at the Leading Edge Region (Non-Linear Model) 47
Figure 4.17. Deformation at the Middle Region (Non-Linear Model) 48
Figure 4.18. Deformation at the Trailing Edge Region (Non-Linear Model)..... 48
Figure 4.19. Von-Mises Strain Result of Elastomeric Chamber of Cell Actuators. 49
Figure 4.20. Von-Mises Strain Result of Elastomeric Chamber of Up2 Actuators 50
Figure 4.21. Von-Mises Stress Result of Aluminum Region of the Morphing Airfoil. 50
Figure 4.22. Von-Mises Stress Result of Aluminum Stiffener of Up2 Actuator.... 51
Figure 4.23. Von-Mises Stress Result of Aluminum Stiffener of Up2 Actuator (Filtered) 52
Figure 4.24. Von-Mises Stress Result of Parts where no Actuators are placed..... 53
Figure 4.25. Linear and Non-Linear Deformation Results 54
Figure 6.1. Deformation of Unit Load Model - LC Up 1 63
Figure 6.2. Deformation of Unit Load Model - LC Up 2 63
Figure 6.3. Deformation of Unit Load Model - LC Up 3 64

Figure 6.4. Deformation of Unit Load Model - LC Up 4 64
Figure 6.5. Deformation of Unit Load Model - LC Mid 1 65
Figure 6.6. Deformation of Unit Load Model - LC Mid 2 65
Figure 6.7. Load Level vs Load Increment Graph 66
Figure 6.8. Displacement Error vs Load Increment Graph 66
Figure 6.9. Load Vector vs Load Increment Graph 67
Figure 6.10. Energy Error vs Load Increment Graph 67

CHAPTER 1

INTRODUCTION

The design of an airfoil is dependent on the intended use and operating conditions, as well as the desired performance characteristics. For different flow interactions, airfoils take different shapes to increase efficiency and performance. Aircraft wings, wind turbine blades or helicopter blades are built using single or multiple airfoil sections that are chosen to meet the specific requirements of the mission. However, these airfoil sections cannot be changed after being built. Engineers select airfoil sections to complete a single mission. “Morphing Structures” concept allows designing a single shape changing airfoil which can complete multiple missions efficiently.

Morphing structures are structures which can change their planforms as a result of a given input. Inspired from the nature, morphing structure allows the system to change its parameters in order to operate better in different circumstances. In air vehicles, the morphing can be applied to the wing structure to improve its capabilities during the flight. Instead of using rigid wing structures, using more flexible and versatile wing designs have many advantages. It provides increment in the efficiency and performance. By introducing a morphing concept, continuous flight control surfaces can be designed resulting to decreased energy loss due to air friction (i.e. drag). These flexible wing designs allow aircraft to adapt to a variety of flight conditions (such as take-off, cruise and landing) by also improving overall mission capabilities[1]

In this study, a morphing wing which changes its profile to a target airfoil is introduced by using fluid actuated cell structures. This allows airfoil profile change

during the mission to increase efficiency, performance and capability of the structures which interact with the fluid flow.

1.1 Background of the Study

In millions of years, nature have learned how to deal with fluid flow. In air, birds have been increasing their capabilities of flight. They evolve in such a way that they can control their wings using muscles to be able to maneuver or increase their flight speed. In Figure 1.1, the various wing shapes of a bird is represented.

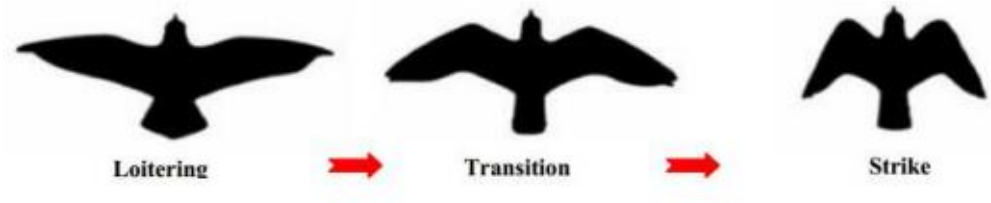

Figure 1.1. Sweep Angle Change of a Bird [2]

Similarly, under water, fish have fins that they can open and close to swim faster and have better maneuver performance. To illustrate, sailfish, the fastest fish in the world, can reach up to 110 km/h and has excellent maneuver capabilities thanks to their big fins at their back. To speed up, they close their fins and at high speeds they open it to make sharp turns.

Engineers always inspire from nature in their designs. Airfoils on many aircraft are designed to resemble the wings of birds. For example, high-speed birds alter the shape of their wings to a dihedral angle to increase their speed and maneuverability. Fighter aircraft also use dihedral wing designs for the same reason. These designs allow the aircraft to move more quickly and agilely through the air. In contrast to high-speed birds, birds that travel long distances have long and slender wings that allow them to glide for extended periods of time without flapping their wings. Engineers who design unmanned aerial vehicles (UAVs) often use high aspect ratio

wings to increase the range and low-speed performance of these vehicles. This allows the UAVs to fly for longer distances without the need to use as much power.

Unlike birds, aircraft are unable to change the shape of their wings during the flight. This means that each aircraft is optimized for a specific mission. To overcome this limitation and improve the efficiency of multi-mission aircraft, engineers are developing “morphing wing” technologies that allow the wings to change shape in flight. Lift and drag values of the aircraft can be modified with the morphing wing designs [3], [4]. This allows the aircraft to adopt to different missions and conditions by also improving its overall performance.

There are many examples of wing morphing in the literature. Bishay and Aguilar [5] have classified these examples into three main categories: airfoil morphing, planform morphing and out of plane morphing. Figure 1.2 shows the list of these different types of morphing.

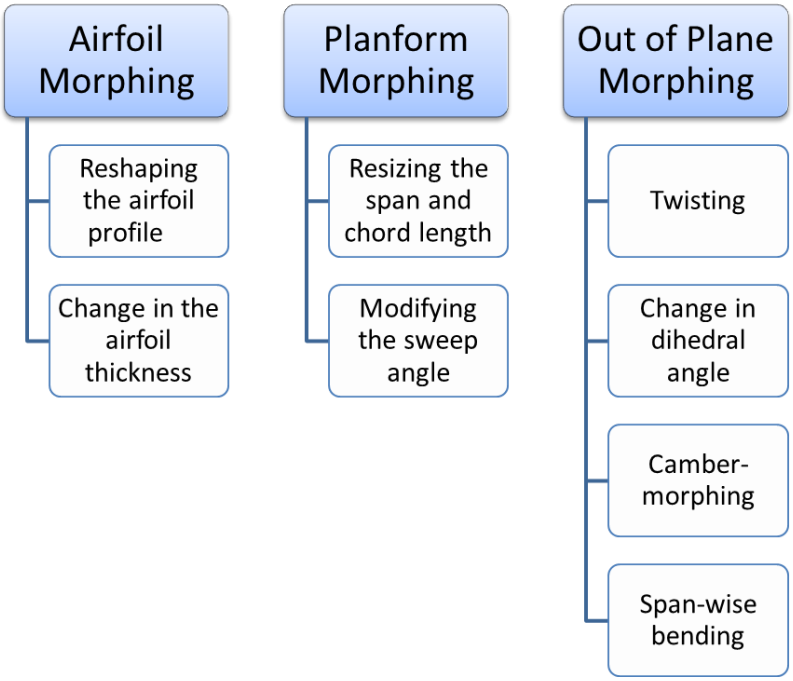

Figure 1.2. Categorization of Morphing Types [5]

There are also several methods to morph structure in the literature and some of these methods use mechanism such as scissor-structural mechanism [6]. As shown in

Figure 1.3, scissor-structural mechanisms are complex and require careful design calculations and additionally, their morphing capabilities are limited. For each target airfoil new scissor-structural mechanism is needed. Some other morphing design methods use servo actuators [7]–[11]. A servo actuator deforms the upper and lower surface of the wing to create morphing as shown in Figure 1.4. These designs are effective for use as control surfaces and can be used to morph the base trailing edge to some target trailing edge profiles. Figure 1.5 shows the capability of the servo actuated morphing trailing edge control surface; however, these actuators are difficult to maintain.

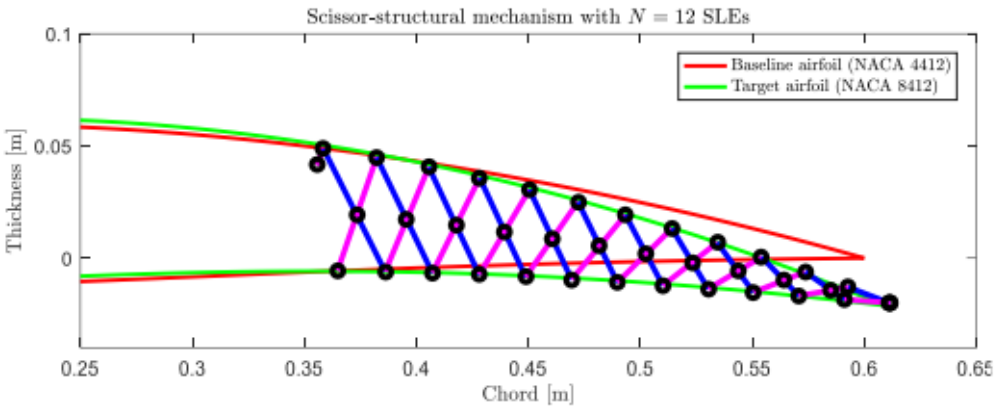

Figure 1.3. Morphing with Scissor-Structural Mechanism [6]

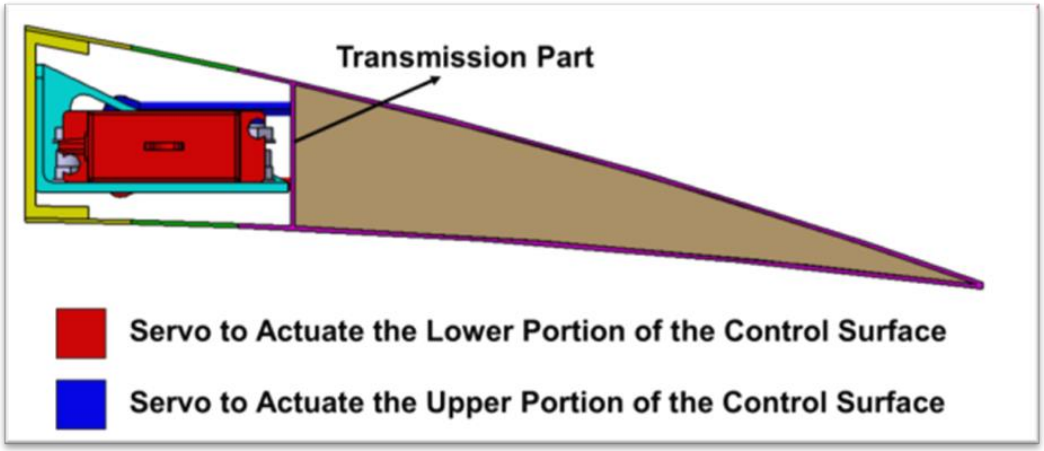

Figure 1.4. Servo Actuated Control Surface [12]

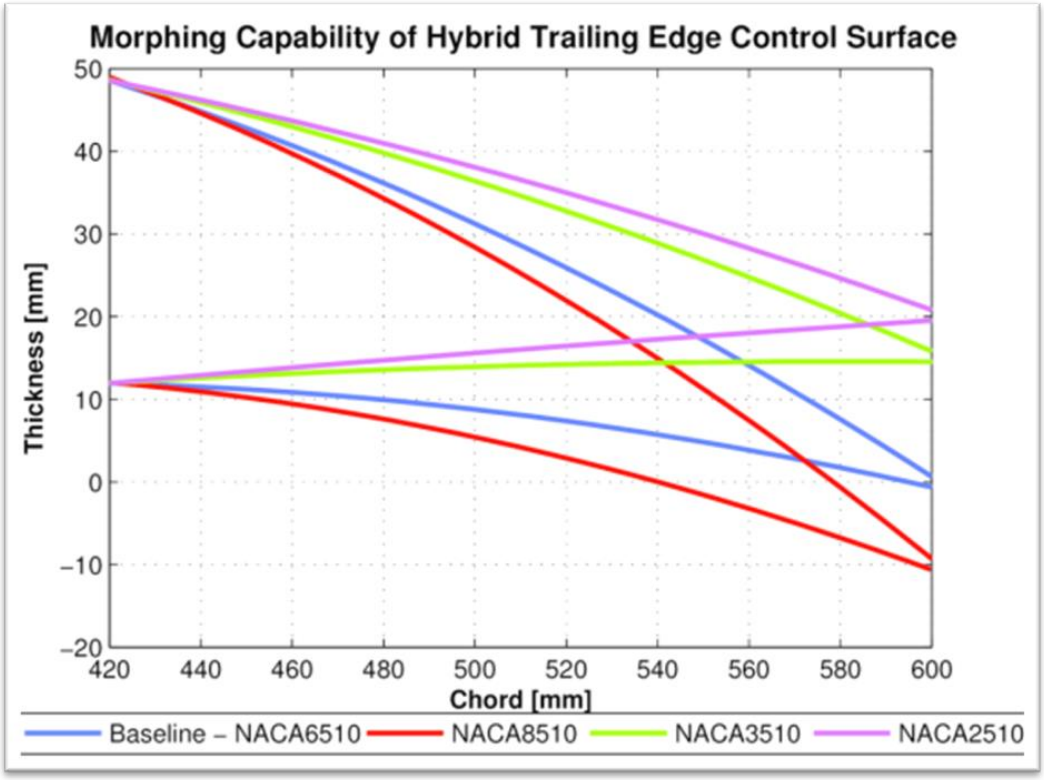

Figure 1.5. Capability of Servo Actuated Control Surface [12]

In contrast to the aforementioned methods, some designs use smart structures such as piezoelectric materials [13], memory shape alloys [13] or composites [14] as the material for morphing structures. These materials are able to change shape in response to electrical or thermal stimuli allowing the structure to morph without the need for external actuators.

Recent studies have shown that using hyperelastic materials, it is possible to design cell structures [15]–[24] that can morph when pressurized. These structures are able to change shape in response to applied pressure allowing them to adapt to different conditions and perform a range of functions.

Fluid actuated morphing structures are structures that can change their geometric parameter to improve the system or vehicle capabilities applying fluid pressure into the structure. The deformation due to internal pressure creates shape change (i.e. morphing) in the structure. Fluid pressure is applied to the sub-structures called “cell

structures” which are typically tube-like in shape and consist of both isotropic and hyperelastic materials. The elastic material (such as aluminum, plastic, etc.) provides stiffness, while hyperelastic material provides shape change with high strain values. Additionally, cell structures can be designed in a wide range of shapes, allowing for greater flexibility in the design of the overall structure. An example of a cell structure is shown in Figure 1.6.

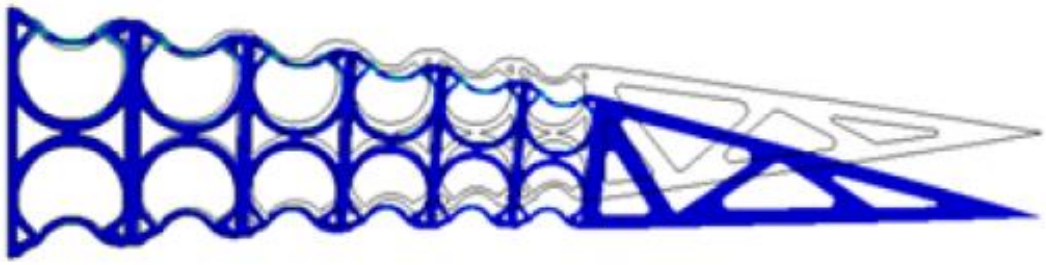

Figure 1.6. A Morphing Trailing Edge Design Using Pressurized Cell Structures [15]

Vasista et al. have studied fluid actuated unit (cell) structures and in their research, they have designed and tested these cell structures [14] using PolyJet materials as the hyperelastic material. Their work has shown that these cell structures are able to undergo large deformations without failure. In their articles, they refer to these structures as fluid actuated morphing unit structures (FAMoUS). Figure 1.7 shows the extension capabilities of a sample cell structure.

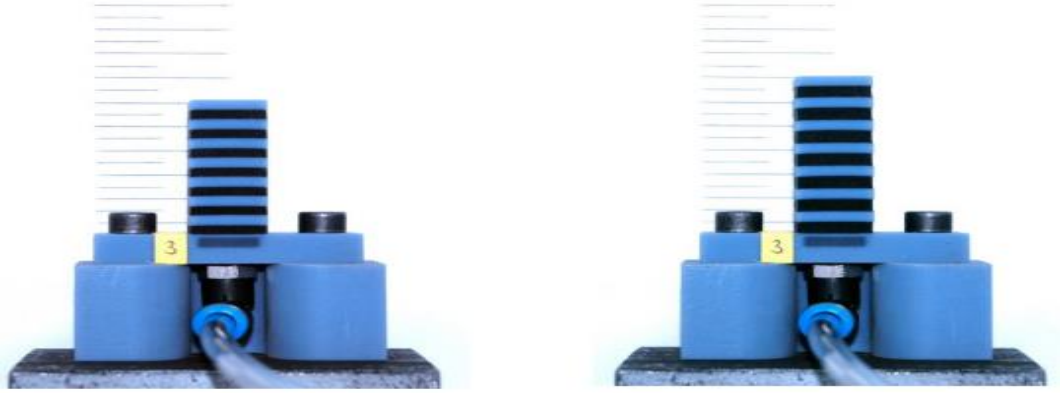

Figure 1.7. Deformation of FAMoUS specimen [21]

Later in the MANTA project [20], Vasista et al. designed a control surface for a wing that can be used as a morphing winglet trailing edge. As shown in Figure 1.8, the trailing edge consists of two units. These units are designed to change shape in response to applied fluid pressure, allowing the winglet to adapt to different conditions and improve its performance.

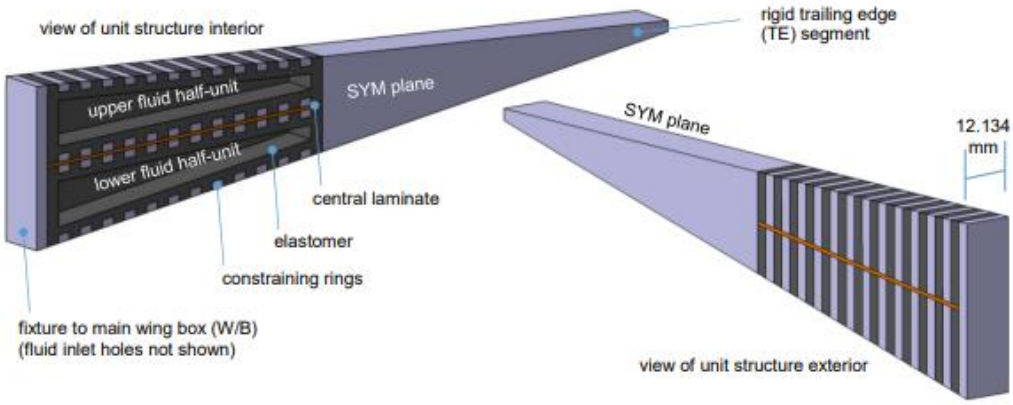

Figure 1.8. Morphing Trailing Edge Design Using FAMoUS [20]

When one of the units is pressurized, the pressurized half unit expands while the other half unit does not. This displacement difference causes the trailing edge structure to bend as seen in Figure 1.9. Case 6 in Figure 1.9 shows the result of a pressurized lower fluid half unit, while case 3 shows the result of a pressurized upper fluid half-unit in a finite element model.

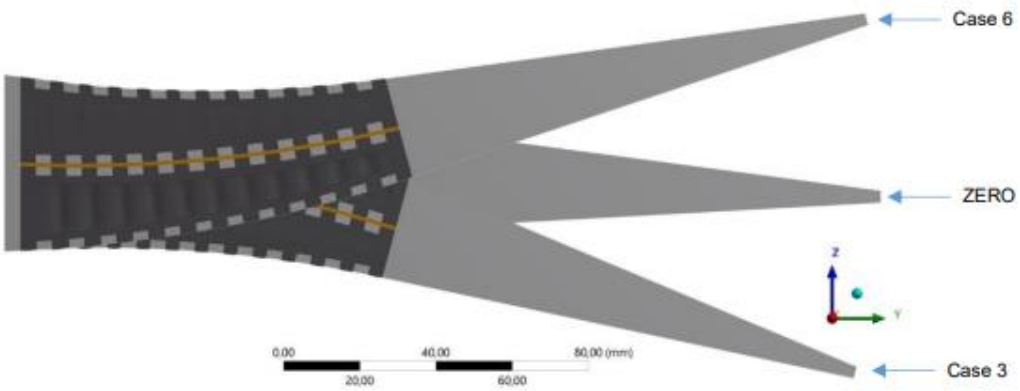

Figure 1.9. Deformation Plot of Finite Element Result of Designed Trailing Edge [20]

In 2018, Vasista et al. [18] designed and printed a trailing edge wing using a 3D printer. The wing was based on a NACA0012 airfoil profile with a chord length of 400 mm and a span of 90 mm. It was equipped with a total of six cells, arranged in three spanwise cells and two cells in height, allowing for bi-cambering, extension, and twist. Figure 1.10 shows the results of the morphing tests on the trailing edge. These results demonstrate that it is possible to design and fabricate structures using cell structures.

Figure 1.10. Deformation of 3D Printed Trailing Edge Specimen [18]

Following the successful design and fabrication of a trailing edge wing, the FAMoUS concept was applied to a more challenging design [18]. A winglet (Figure 1.11) was designed, manufactured and then pressurized to demonstrate its morphing capabilities. This design shows that the FAMoUS concept can be applied to more complex structures, and that it can be used to create effective morphing wings.

Figure 1.11. 3D Winglet Specimen Built Using Pressurized Cell Structures [18]

1.2 Motivation and Objective of the Study

As seen in the literature, there are many different morphing concepts that have been introduced. Some of these concepts use scissor-structural mechanisms while the others use servo actuators, smart structures or composite materials. However, the capabilities of these methods are limited. For example, scissor-structural mechanisms are complex and require careful design, while servo actuators are difficult to maintain. These limitations make it challenging to develop effective morphing structures.

Additionally, much of the literature on morphing focuses on trailing edge morphing and leading edge (i.e. droop nose) morphing. In contrast, airfoil morphing is capable of changing a wide range of parameters on an airfoil. Furthermore, the concept of pressurized cell structures is relatively new and there are limited number of studies on this topic compared to other morphing concepts, such as mechanisms and servo actuators. This means that there is still much to be explored on the potential of pressurized cell structures for morphing applications.

Therefore, the aim of this thesis is to contribute to the growing body of knowledge on fluid actuated morphing concepts by demonstrating that it is possible to morph an airfoil profile (so called a baseline) into another one (a target one). To achieve this goal, a targeting algorithm is needed to calculate the pressure distribution in the cell structures (i.e. cell actuators). Therefore, another objective of this study is to develop this algorithm that can be used to control the morphing action of the airfoil. Through this work, the understanding of pressurized cell structures and their potential applications in morphing technologies will also be ameliorated.

1.3 Outline of the Study

The organization of this thesis is as follows:

Chapter 1 provides an introduction to the study, including background information and a literature review on morphing structures. The motivation, objectives, and limitations of the study are also discussed in this chapter.

Chapter 2 provides an overview of airfoils and explains the key parameters that are used to describe their shape and performance. The design parameters for the morphing airfoil and the materials used in the case studies are discussed.

Chapter 3 describes finite element modeling using unit loads and provides the details of the targeting algorithm. This chapter also includes a detailed description of the calculations used in the algorithm to determine the pressure distribution in the cell structures.

Chapter 4 presents the results of linear and non-linear finite element simulations, including the final pressure distribution that is used to control the morphing of the airfoil. The implication and comparison of these results to expectations are also discussed.

Chapter 5 provides general conclusions and discusses the potential applications and future directions for this research by presenting recommendations for further work on fluid actuated morphing structures.

CHAPTER 2

DESIGN OF MORPHING AIRFOILS

2.1 Introduction

In this chapter, the design process of a fluid-actuated morphing airfoil is presented. The chapter begins by describing the main parameters of an airfoil and introducing NACA airfoils and their naming conventions. The cell structures used for the morphing airfoil are then explained, followed by a discussion of the materials chosen for the cell structures. The chapter then goes on to describe the placement of the pressure-driven cell structures in detail and presents the final design of the morphing airfoil.

2.2 Baseline Airfoil Selection for the Morphing Application

There are many important airfoil parameters that directly affect the lift, drag and moment created by the airfoil itself. These parameters include the chord, maximum thickness, thickness to chord ratio, maximum camber and maximum camber location, as shown in Figure 2.1.

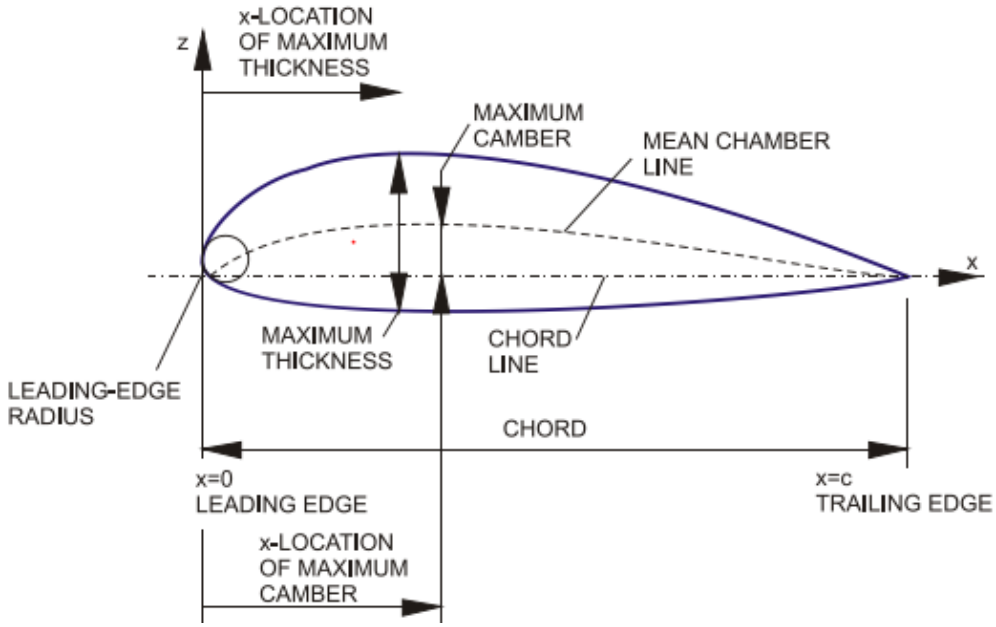

Figure 2.1. Main Geometric Parameters of an Aerodynamic Airfoil [25]

The National Advisory Committee for Aeronautics (NACA) developed airfoil shapes for aircraft wings. These airfoil profiles are described using a series of digits following the word "NACA". All four-digit NACA airfoils have a chord length between 0 and 1.00. The first digit gives the percentage maximum camber of the airfoil, the second digit gives the location of the maximum camber along the chord, and the third and fourth digits give the percentage thickness of the airfoil. For example, the NACA 6412 airfoil has a maximum camber of 6% at 39.6% (~40%) of the chord and a maximum thickness of 12%.

In this study, a design for a morphing airfoil is presented. This airfoil is aimed to be capable of changing its profile to another NACA profile. For the baseline airfoil design, NACA 0012 profile, which is a well-known symmetric airfoil profile in the literature is selected. The aim is to use the NACA 0012 profile to design a morphing airfoil that can be transformed into another profile, such as NACA 2412 using fluid-actuated cell structures.

To begin the design of the morphing airfoil, first, an airfoil with a 500 mm chord that is a suitable chord for testing in a conventional wind tunnel is generated using Altair®

HyperWorks Workbench v2019.1. Since the NACA 0012 profile is used for the baseline airfoil design, its maximum thickness is 60 mm. The cross-section of the airfoil is 8 mm x 8 mm, as shown in Figure 2.2.

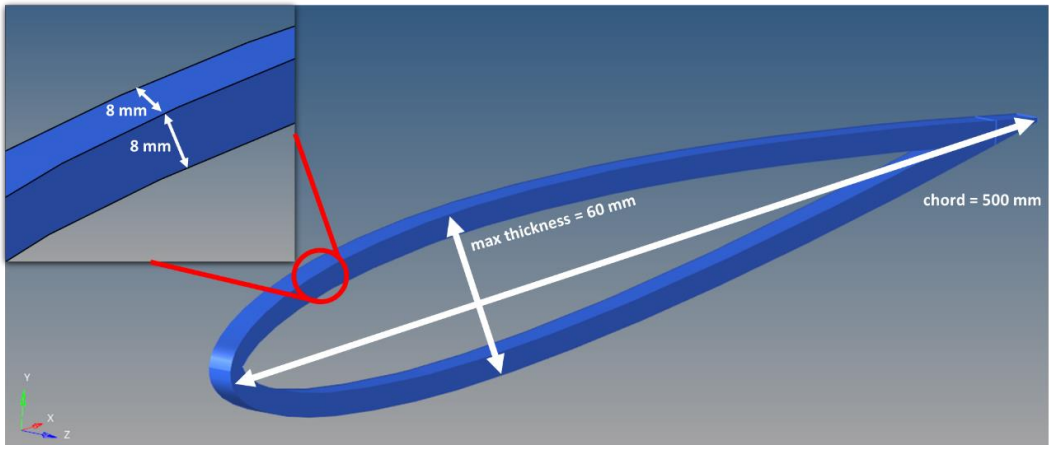

Figure 2.2. The Morphing Airfoil Without Cell Structures

After the airfoil is drawn, spars are added to the design at the 25%, 50%, and 75% of the chord locations. These locations are chosen in order to ensure the morphing of the structure. The spar locations will be responsible for changing the thickness of the airfoil. Figure 2.3 shows the locations of the spars in the morphing airfoil design.

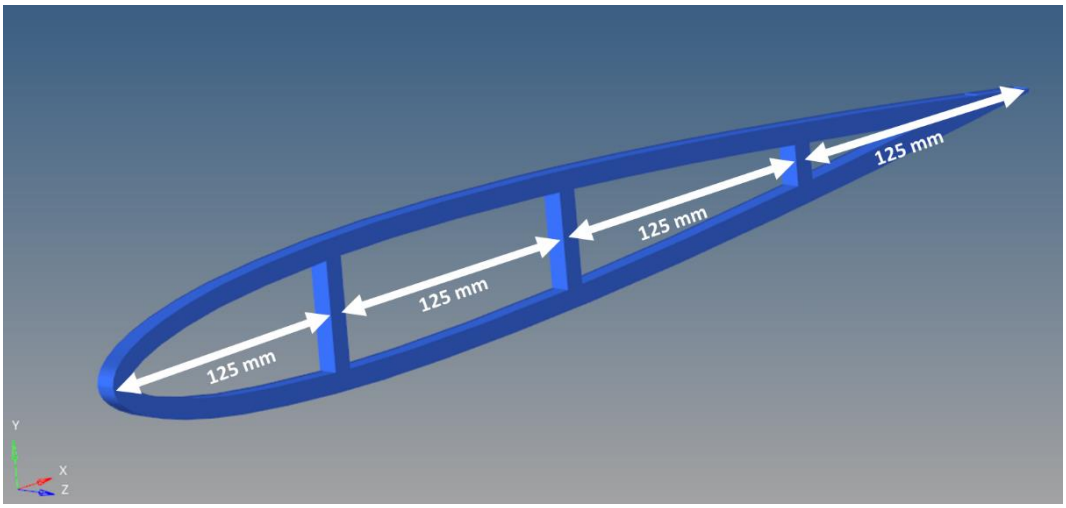

Figure 2.3. Spar Locations of the Morphing Airfoil

2.3 Fluid Actuated Cell Design for the Morphing Airfoil

In order to enable morphing of the airfoil, fluid-actuated cell structures are used in this study. Vasista et al. [18] describe "Fluid Actuated Morphing Unit Structures" (FAMoUS) that are capable of elongating a unit structure axially with minimal outer transverse deformation. This requires an orthotropic arrangement of stiffness with low axial stiffness and high transverse stiffness. This can be achieved using a particular material combination consisting of an elastomeric matrix and stiffer ring constraints. Figure 2.4 shows an example of a FAMoUS in a prismatic shape. The black parts represent the elastomeric material whereas the blue parts represent the stiff material. When subjected to internal pressure, the elastomeric material provides axial elongation while the stiff material prevents outer transverse deformation. Figure 2.5 shows the working principle of fluid-actuated cell designs.

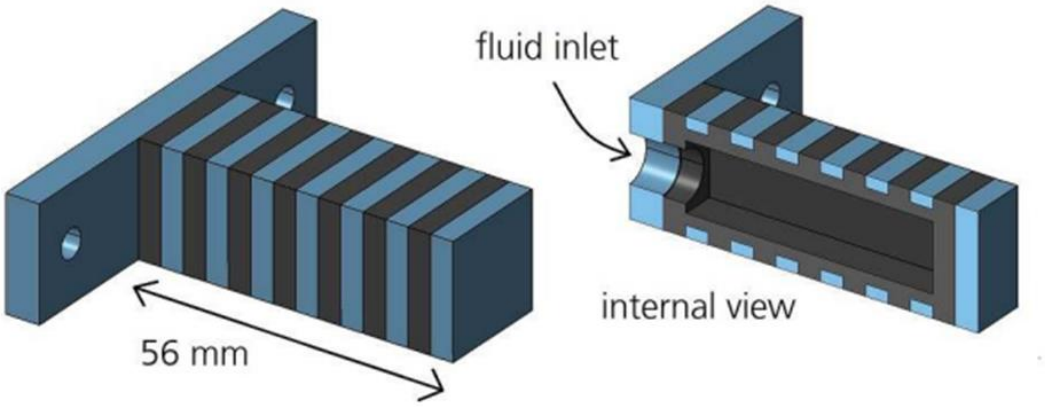

Figure 2.4. Simple Prismatic Cell Design [18]

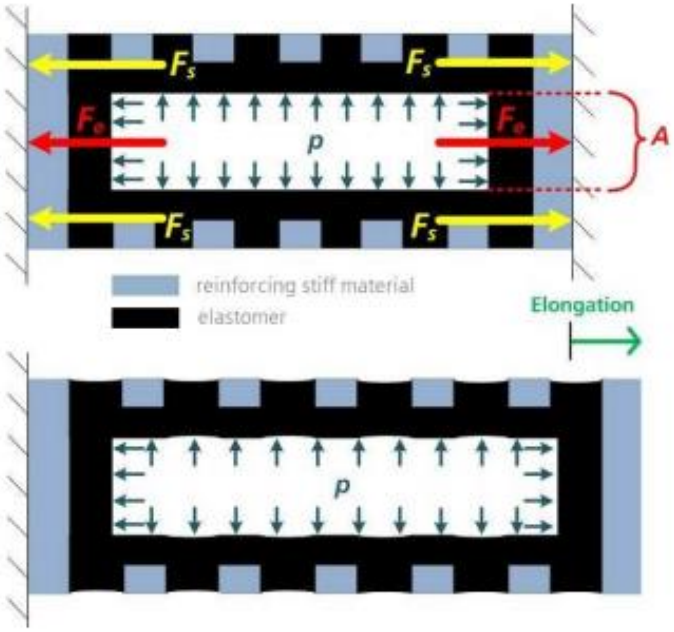

Figure 2.5. Force and Stoke Generation of the FAMoUS Concept [18]

Presented morphing cell concept in Figure 2.5 is used in this study to provide axial elongation for airfoil morphing. In this study, the cell parts of the airfoil design are referred to as "actuators." The designed morphing airfoil uses cells with an 8 mm x 8 mm cross-section, and the elastomer and stiffening ring thickness is 1 mm. The stiffening rings are spaced 2.4 mm apart. Figure 2.6 shows the cell actuator design for the morphing airfoil, with the elastomer material represented in red and the stiff material represented in blue.

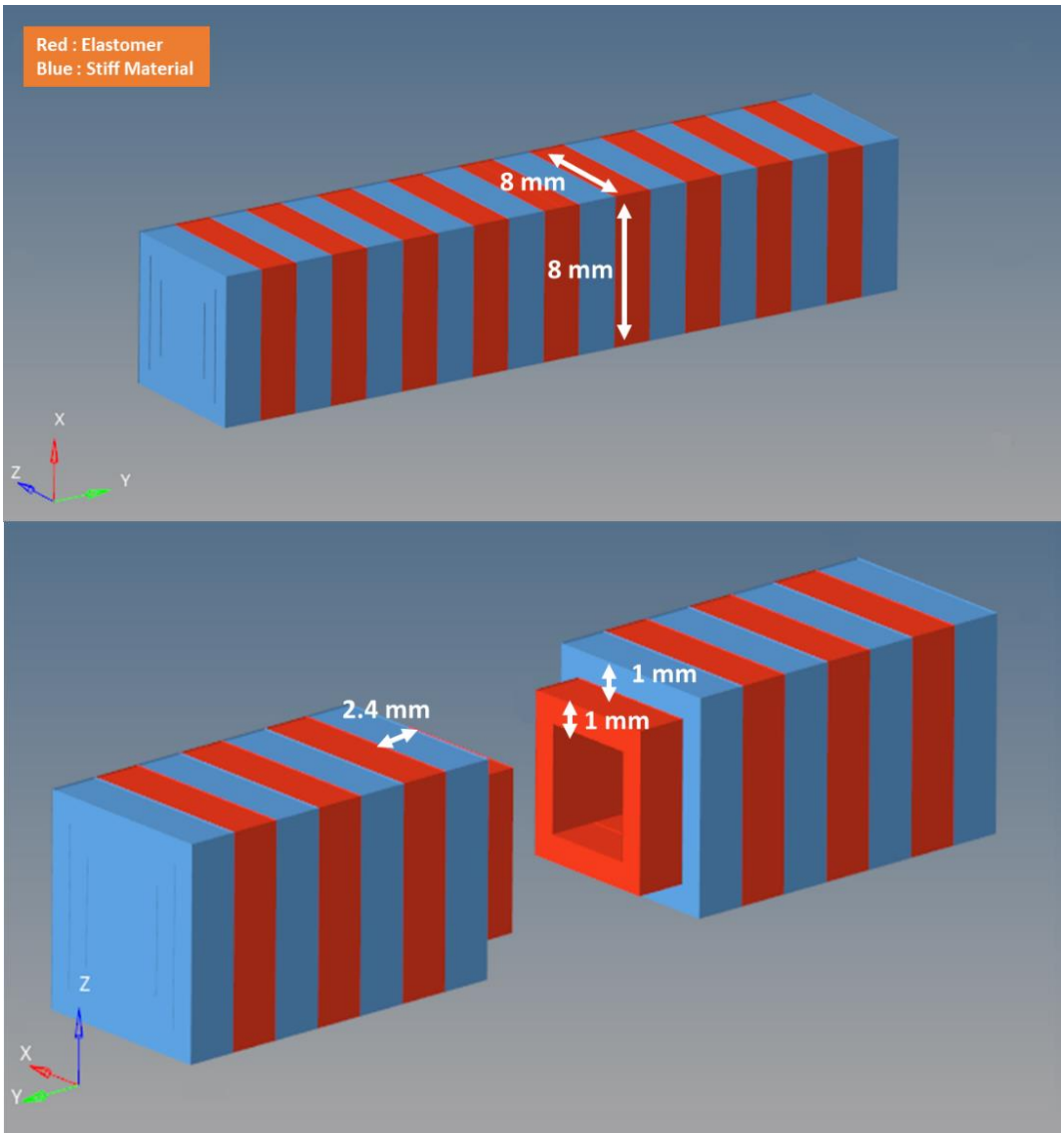

Figure 2.6. Dimensions of the Cell Actuator for Designed Morphing Airfoil

The thickness, cross-section, and stiffening ring spacing are constant for all actuators used in this study. However, the length of the cell actuators depends on the region of the airfoil where they are located. In the upper and lower parts of the airfoil, the cell actuators are formed into a curved shape.

2.4 Material Selection of the Morphing Airfoil

As mentioned in previous chapters, the cell actuator should contain both an elastomeric material (such as a hyper-elastic material) and a stiff material. Aluminum, a commonly used material in the aviation industry, is chosen as the stiff material used in the rings for the cell actuators. The sections of the airfoil that do not contain actuators are also made of aluminum. For the hyper-elastic part of the cell actuators, a Shore A hardness value of approximately 55 for a soft class elastomeric material is used, similar to what was used in the studies of Vasista et al. [18]. The elongation required for the morphing airfoil is provided by this hyper-elastic material.

2.5 Placement of the Cell Actuators

In order to transform one airfoil into another one, the cell actuators should be placed in particular locations that directly affect the airfoil properties. To change the thickness or thickness-to-chord ratio, the spar locations are replaced with cell actuators. As seen in Figure 2.7, the first and the second spar locations from the leading edge are replaced with cell actuators. The third spar is not replaced because of its short length. Very small size actuators may not work properly because there will not be enough hyper-elastic material to allow for elongation.

In addition to changing the thickness, the camber of the airfoil must also be changed in order to reach a desired target airfoil profile. To achieve this, the upper and lower parts of the designed airfoil are replaced with cell actuators. When the upper and lower parts of the airfoil are replaced with a single cell actuator, the camber location cannot be adjusted. To adjust the camber location of the airfoil, the cell actuators are separated. This allows each cell actuator to be pressurized independently, allowing the camber location to be changed. As seen in Figure 2.7, both the upper and lower parts of the airfoil are divided into four actuator regions. These are the leading edge to the first spar, the first spar to the second spar, the second spar to the third spar,

and the third spar to the trailing edge. With these eight cell actuators, the amount of camber at the desired camber location can be adjustable.

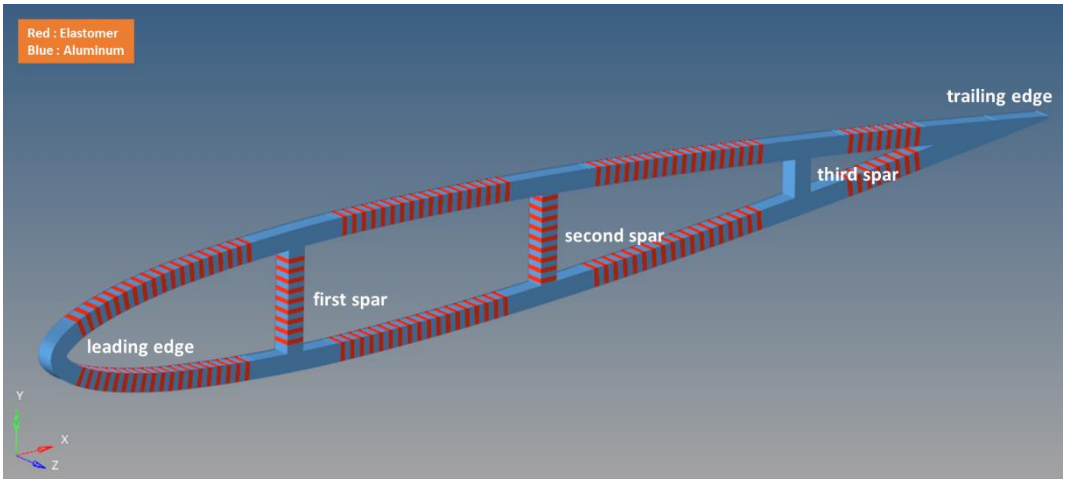

Figure 2.7. Upper and Lower Cell Actuator Locations

For the rest of the study, the cell actuators in the upper region will be referred to as "Up1", "Up2", "Up3" and "Up4" in order from the leading edge to the trailing edge. The actuators in the lower region will be referred to as "Down1", "Down2", "Down3" and "Down4" again in order from the leading edge to the trailing edge as shown in Figure 2.8. The spar actuators will be named "Mid1", "Mid2" and "Mid3" again in order from the leading edge to the trailing edge.

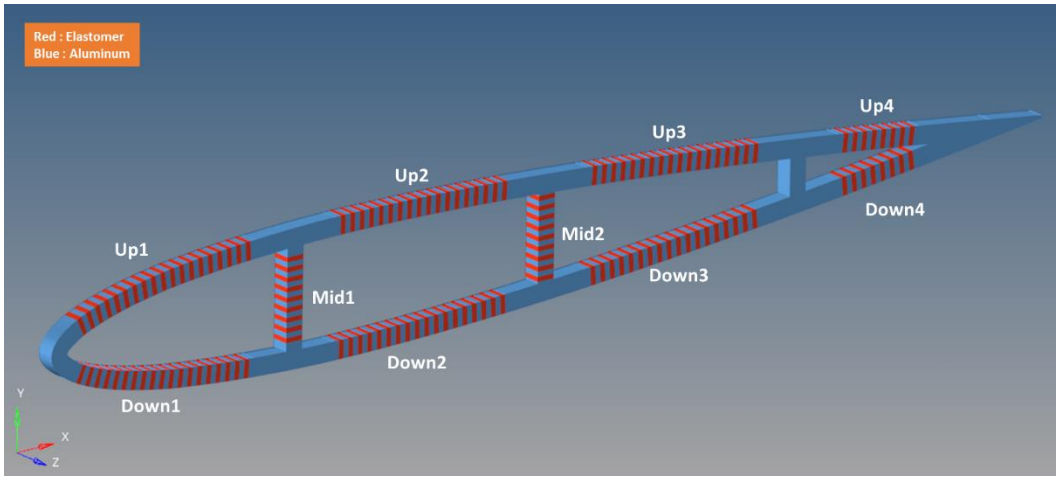

Figure 2.8. Naming of the Cell Actuators

2.6 Conclusions

This chapter describes the design steps of the morphing airfoil. To achieve a successful morphing, separate cell actuator locations are necessary. In the presented morphing airfoil design for each upper and lower part, four cell actuators are located to achieve camber and adjust maximum camber location. On the other hand, there are two more cell actuators located at the 25 % and 50 % chord locations as a spar responsible from adjusting the thickness of the airfoil.

CHAPTER 3

UNIT LOAD METHOD AND TARGETING ALGORITHM

3.1 Introduction

In this chapter, the unit load method and targeting algorithm with the FE model of the designed morphing airfoil is presented. The details of the FE model, including the mesh element type and size are described followed by an explanation of the material modeling. After the airfoil is modeled, the boundary conditions of the model are given and the unit load method is introduced. The loading for the unit load model is then described. Using the results from the unit load model, a targeting algorithm is created using Microsoft® Excel. At the end, the algorithm is used to calculate the pressure distribution requires to morph the baseline airfoil into the target airfoil.

3.2 Details of Finite Element Modelling

A finite element (FE) model of the designed airfoil is created using the Altair® HyperWorks program. The first step in the modeling process is meshing. For this study, second-order tetramesh (tetra10) elements with a mesh size of 1.2 mm are used. This ensures that there are at least two elements per stiffening ring spacing of the cell actuators, as seen in Figure 3.1. A model containing 405295 tetra10 elements and 609555 nodes is created. A 0.75 mm mesh-sized model having 1795606 tetra10 elements and 2542281 nodes is also prepared for comparison purposes. This comparison which presents the displacement results for the two models differ by approximately 5% but it takes 12 times longer to run is given in Appendix A. Therefore, the 1.2 mm mesh size is chosen for the further FE analysis.

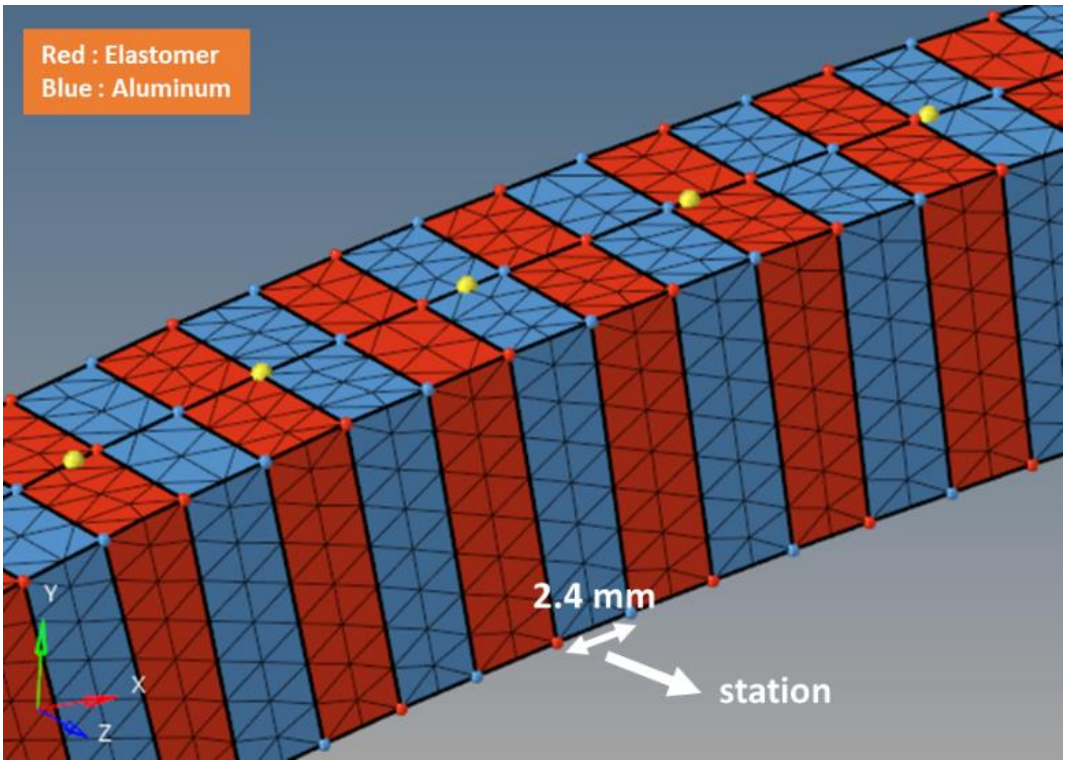

Figure 3.1. Discretication used for Up1 Cell Actuator

Having completed the mesh generation, material properties are assigned to the mesh. For aluminum, a linear isotropic model is used with an elastic modulus of 70000 MPa and a Poisson's ratio of 0.3. For the elastomer, a simple non-linear neo-Hookean hyperelastic material model with initial shear modulus μ_0 of 1 MPa making Neo-Hookean parameter C_{10} value 0.5 MPa as shown in Equation 3.1 [26] and incompressibility factor d_1 of zero is used [18].

$$\mu_0 = 2C_{10} \qquad (Eqn\ 3.1)$$

For the linear FE analysis, Altair® OptiStruct solver linearizes the non-linear neo-Hookean hyperelastic material model. On the other hand, for the non-linear FE analysis, the solver uses directly the Neo-Hookean material model.

At the end, boundary conditions are defined for the model and then it is constrained from the middle line of the first spar, allowing for morphing. As shown in Figure

3.2, all nodes on the mid-line of the first spar are constrained in all translation and rotation directions.

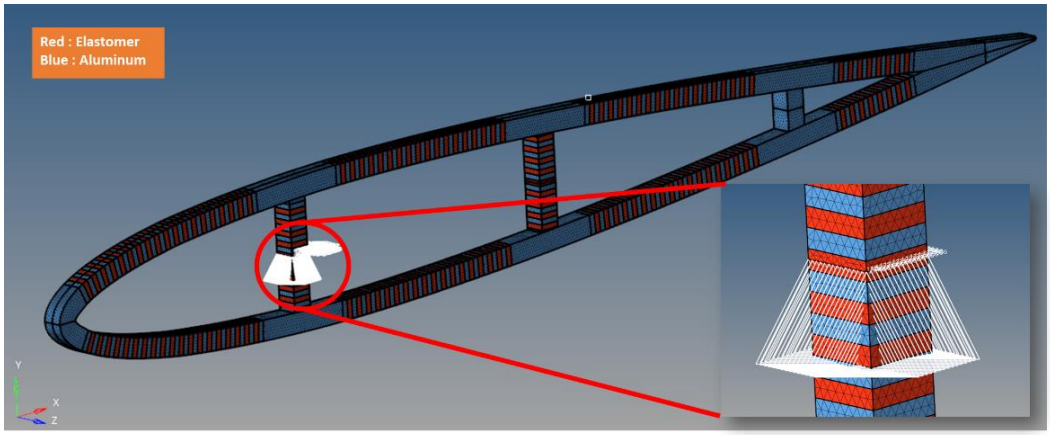

Figure 3.2. Constraints Locations

3.3 Linear Static Finite Element Analysis of Designed Airfoil with Unit Loads

The aim of this study is to morph baseline airfoil by applying pressure to cell actuators in such a way that the final deformed shape becomes a target airfoil profile. To achieve this goal, the first step is the calculation of the pressure inputs for each cell actuators through the unit load method. Unit load method simply uses linear superposition principle which states that when two or more applied loads overlap, the FE results (deformation, stress and strain) are equal to the algebraic sum of the individual FE results. Since superposition method is applicable for linear static FE analysis, an FE model for the designed morphing airfoil is used to create inputs for targeting algorithm which calculates the required pressure distribution.

To superimpose the FE analysis results, unit load subcases are prepared. In each subcase, a pressure of 1 MPa is applied to one of the cell actuators. Since the morphing airfoil has 10 actuators, 10 individual unit load cases are prepared. Figure 3.3 shows the unit load model with a load case in which a pressure of 1 MPa is applied to the Up1 cell actuator.

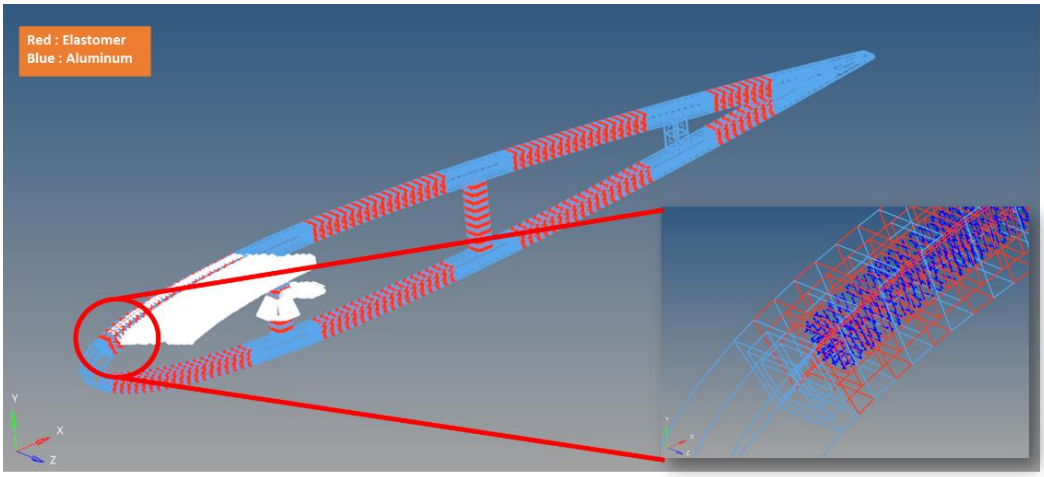

Figure 3.3. Unit Load Case for Up1 Actuator

The linear static unit load model is prepared using Altair® HyperWorks. Also, as a solver Altair® OptiStruct is used. The solution of the model shows the effect of 1 MPa internal pressure on each cell actuator of the morphing airfoil. A post-processing program, Altair® HyperView, is then used to generate a report containing nodal displacement data for the airfoil model. This data is also organized in a Microsoft® Excel sheet for superimposition.

3.4 Targeting Algorithm

The targeting algorithm calculates a linear combination of pressure inputs that result in the minimum difference between the target airfoil and the deformed airfoil. By superimposing the results of the unit load model for the morphing airfoil, the final deformed airfoil results (i.e. deformation, stress, strain) are obtained. For simplicity, only the deformed X and Y coordinate data of 20 nodes is selected from the nodal information obtained from the unit load model. These nodes are chosen on the start and end point of the upper and lower cell actuators, as well as the leading and trailing edges of the designed airfoil, as shown in Figure 3.4.

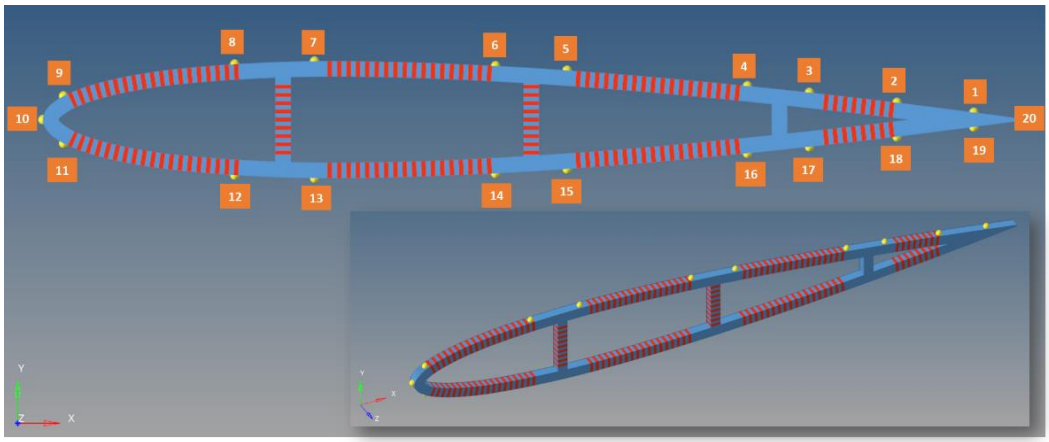

Figure 3.4. Selected Nodes (yellow)

Below Table 3.1 and Table 3.2 show that the undeformed and deformed coordinates of the selected nodes named as seen in Figure 3.4. “LC Up1” shows that the Unit Load method deformed coordinates of load case (LC) where only the Up1 cell actuator is pressurized by 1 MPa internal pressure.

Table 3.1 Undeformed and Deformed X Coordinates of Selected Nodes

X [mm]	Undeformed	LC Up1	LC Up2	LC Up3	LC Up4	LC Down1	LC Down2	LC Down3	LC Down4	LC Mid1	LC Mid2
1	476.46	476.45	480.55	480.73	478.56	476.49	479.47	479.31	477.27	476.38	476.23
2	437.11	437.07	441.93	442.33	440.09	437.16	439.39	439.01	437.04	437.02	436.88
3	392.28	392.22	397.85	398.48	392.28	392.37	393.82	393.21	392.28	392.19	392.06
4	360.58	360.49	366.63	367.41	360.58	360.68	361.63	360.87	360.58	360.48	360.35
5	268.28	268.15	275.44	268.29	268.28	268.44	268.23	268.28	268.29	268.20	268.19
6	231.65	231.50	239.11	231.69	231.65	231.82	231.29	231.62	231.65	231.58	231.56
7	139.05	138.85	139.20	139.07	139.05	139.28	138.93	139.05	139.05	138.98	138.89
8	98.18	97.81	98.30	98.19	98.18	98.41	98.07	98.18	98.18	98.10	98.03
9	10.57	4.62	10.60	10.57	10.57	9.06	10.55	10.57	10.57	10.76	10.40
10	0.00	-3.73	0.01	0.00	0.00	-3.73	0.01	0.01	0.00	0.20	-0.17
11	10.57	9.06	10.55	10.57	10.57	4.61	10.60	10.58	10.57	10.78	10.40
12	98.18	98.42	98.07	98.17	98.18	97.80	98.31	98.19	98.18	98.17	98.03
13	139.05	139.28	138.93	139.05	139.05	138.84	139.20	139.07	139.05	139.05	138.89
14	231.65	231.82	231.29	231.62	231.65	231.50	239.11	231.69	231.65	231.64	231.57
15	268.28	268.44	268.23	268.28	268.29	268.14	275.43	268.29	268.28	268.25	268.19
16	360.58	360.68	361.63	360.87	360.58	360.48	366.62	367.41	360.58	360.52	360.35
17	392.28	392.37	393.82	393.21	392.28	392.21	397.85	398.48	392.28	392.22	392.05
18	437.11	437.17	439.39	439.01	437.04	437.06	441.92	442.33	440.09	437.04	436.88
19	476.46	476.49	479.47	479.31	477.27	476.44	480.55	480.73	478.57	476.39	476.23
20	500.00	500.01	503.55	503.56	501.46	500.01	503.55	503.56	501.46	499.93	499.77

Table 3.2 Undeformed and Deformed Y Coordinates of Selected Nodes

Y [mm]	Undeformed	LC Up1	LC Up2	LC Up3	LC Up4	LC Down1	LC Down2	LC Down3	LC Down4	LC Mid1	LC Mid2
1	3.73	6.44	-37.89	-29.50	-7.14	1.00	45.37	36.97	14.60	4.17	3.75
2	8.74	11.23	-27.17	-17.02	4.73	6.24	44.68	34.52	12.76	9.14	8.77
3	13.89	16.13	-15.52	-3.36	13.89	11.64	43.33	31.17	13.89	14.24	13.92
4	17.23	19.29	-7.58	6.00	17.23	15.16	42.07	28.49	17.23	17.54	17.26
5	25.24	26.75	13.46	24.15	25.24	23.72	37.08	26.35	25.23	25.31	26.67
6	27.51	28.79	20.70	26.87	27.51	26.21	34.32	28.11	27.51	27.83	29.04
7	29.92	30.17	29.76	29.91	29.92	29.66	30.08	29.93	29.92	31.45	30.06
8	28.38	27.99	28.63	28.41	28.38	28.81	28.15	28.37	28.38	29.76	28.19
9	12.10	1.45	12.80	12.16	12.10	22.73	11.40	12.04	12.10	11.94	12.10
10	0.00	-12.59	0.72	0.06	0.00	12.57	-0.73	-0.06	0.00	-0.17	0.00
11	-12.10	-22.75	-11.41	-12.04	-12.10	-1.47	-12.80	-12.16	-12.10	-12.26	-12.10
12	-28.38	-28.81	-28.15	-28.37	-28.38	-27.98	-28.64	-28.41	-28.38	-29.85	-28.19
13	-29.92	-29.66	-30.07	-29.93	-29.92	-30.17	-29.76	-29.91	-29.92	-31.39	-30.06
14	-27.51	-26.22	-34.28	-28.12	-27.51	-28.80	-20.65	-26.86	-27.51	-27.48	-29.01
15	-25.24	-23.72	-37.04	-26.35	-25.23	-26.76	-13.43	-24.16	-25.24	-24.88	-26.63
16	-17.23	-15.17	-42.04	-28.46	-17.23	-19.30	7.61	-5.96	-17.23	-16.91	-17.20
17	-13.89	-11.65	-43.30	-31.14	-13.89	-16.14	15.55	3.39	-13.89	-13.54	-13.86
18	-8.74	-6.25	-44.66	-34.50	-12.76	-11.25	27.19	17.04	-4.73	-8.35	-8.72
19	-3.73	-1.01	-45.35	-36.96	-14.60	-6.45	37.92	29.51	7.15	-3.29	-3.70
20	0.00	2.85	-45.04	-37.70	-14.97	-2.86	45.06	37.71	14.98	0.46	0.02

Using Equation 3.2, X and Y nodal displacements are calculated from presented deformed coordinate and undeformed coordinate data of selected nodes under each unit load case, then are tabulated as seen in Table 3.3 and Table 3.4. Unit load cases have the same name with corresponding cell actuators.

$$\delta X = X_{Act} - X_{Undeformed} \quad and \quad \delta Y = Y_{Act} - Y_{Undeformed} \qquad (Eqn\ 3.2)$$

for each selected node and Act is unit load case of corresponding cell actuator.

Table 3.3 X displacements of Unit Load Cases

δX [mm]	**LC Up1**	**LC Up2**	**LC Up3**	**LC Up4**	**LC Down1**	**LC Down2**	**LC Down3**	**LC Down4**	**LC Mid1**	**LC Mid2**
1	-0.01	4.09	4.27	2.11	0.03	3.01	2.86	0.81	-0.08	-0.23
2	-0.04	4.82	5.22	2.98	0.06	2.28	1.90	-0.07	-0.08	-0.23
3	-0.07	5.57	6.20	0.00	0.08	1.53	0.93	0.00	-0.09	-0.23
4	-0.09	6.05	6.83	0.00	0.10	1.05	0.30	0.00	-0.09	-0.23
5	-0.14	7.15	0.01	0.00	0.15	-0.05	0.00	0.00	-0.08	-0.10
6	-0.15	7.46	0.03	0.00	0.17	-0.36	-0.03	0.00	-0.07	-0.09
7	-0.21	0.14	0.02	0.00	0.23	-0.13	0.00	0.00	-0.07	-0.17
8	-0.37	0.12	0.01	0.00	0.23	-0.11	0.00	0.00	-0.08	-0.15
9	-5.95	0.03	0.01	0.00	-1.51	-0.02	0.00	0.00	0.19	-0.17
10	-3.73	0.01	0.00	0.00	-3.73	0.01	0.01	0.00	0.20	-0.17
11	-1.51	-0.02	0.00	0.00	-5.96	0.03	0.01	0.00	0.21	-0.17
12	0.24	-0.11	-0.01	0.00	-0.38	0.13	0.01	0.00	-0.01	-0.15
13	0.23	-0.13	-0.01	0.00	-0.21	0.14	0.02	0.00	0.00	-0.17
14	0.17	-0.36	-0.03	0.00	-0.16	7.45	0.03	0.00	-0.01	-0.09
15	0.16	-0.05	0.00	0.00	-0.14	7.15	0.01	0.00	-0.03	-0.09
16	0.11	1.05	0.29	0.00	-0.09	6.05	6.83	0.00	-0.06	-0.23
17	0.09	1.54	0.92	0.00	-0.07	5.56	6.20	0.00	-0.06	-0.23
18	0.06	2.28	1.90	-0.07	-0.04	4.82	5.22	2.98	-0.06	-0.23
19	0.03	3.01	2.85	0.81	-0.01	4.09	4.27	2.11	-0.07	-0.23
20	0.01	3.55	3.56	1.46	0.01	3.55	3.56	1.46	-0.07	-0.23

Table 3.4 Y displacements of Unit Load Cases

δY [mm]	**LC Up1**	**LC Up2**	**LC Up3**	**LC Up4**	**LC Down1**	**LC Down2**	**LC Down3**	**LC Down4**	**LC Mid1**	**LC Mid2**
1	2.71	-41.62	-33.23	-10.87	-2.73	41.64	33.24	10.88	0.44	0.02
2	2.49	-35.91	-25.76	-4.01	-2.50	35.94	25.78	4.01	0.40	0.03
3	2.24	-29.41	-17.25	0.00	-2.25	29.44	17.28	0.00	0.35	0.03
4	2.06	-24.81	-11.23	0.00	-2.07	24.84	11.26	0.00	0.32	0.03
5	1.52	-11.77	-1.08	0.00	-1.52	11.85	1.11	0.00	0.08	1.44
6	1.28	-6.80	-0.64	0.00	-1.29	6.81	0.60	0.00	0.32	1.54
7	0.24	-0.16	-0.02	0.00	-0.26	0.15	0.01	0.00	1.53	0.14
8	-0.39	0.25	0.02	0.00	0.42	-0.23	-0.01	0.00	1.38	-0.20
9	-10.65	0.69	0.06	0.00	10.63	-0.70	-0.06	0.00	-0.16	0.00
10	-12.59	0.72	0.06	0.00	12.57	-0.73	-0.06	0.00	-0.17	0.00
11	-10.65	0.69	0.06	0.00	10.63	-0.70	-0.06	0.00	-0.16	0.00
12	-0.43	0.23	0.02	0.00	0.41	-0.25	-0.03	0.00	-1.46	0.19
13	0.26	-0.15	-0.01	0.00	-0.25	0.16	0.02	0.00	-1.46	-0.13
14	1.29	-6.77	-0.61	0.00	-1.29	6.85	0.64	0.00	0.03	-1.51
15	1.51	-11.81	-1.11	0.00	-1.52	11.81	1.07	0.00	0.35	-1.39
16	2.06	-24.81	-11.23	0.00	-2.07	24.84	11.26	0.00	0.32	0.03
17	2.24	-29.41	-17.25	0.00	-2.25	29.44	17.28	0.00	0.35	0.03
18	2.49	-35.91	-25.76	-4.01	-2.50	35.94	25.78	4.01	0.40	0.03
19	2.71	-41.62	-33.23	-10.87	-2.73	41.64	33.24	10.88	0.44	0.02
20	2.85	-45.04	-37.70	-14.97	-2.86	45.06	37.71	14.98	0.46	0.02

By using Equation 3.3, the final linearly superimposed deformation is calculated for both X and Y coordinate for each selected node.

$$\delta X = \sum_{i=1}^{10} \delta X_i kp_i \quad and \quad \delta Y = \sum_{i=1}^{10} \delta Y_i kp_i \qquad (Eqn 3.3)$$

where, *i* is unit case id and *kp* is pressure coefficient

Then, the calculated deformation is added to the undeformed coordinates to find the deformed coordinates of the airfoil. At the end, the deformed airfoil has some angle of attack. However, NACA 0012 and NACA 2412 airfoil data are at zero angle of attack position. To calculate the angle of attack, the position of the leading-edge node (node 10) and the trailing edge node (node 20) in the deformed state is used as seen in Equation 3.4.

$$Angle\ of\ Attack = \arctan\left(\frac{Y_{20} - Y_{10}}{X_{20} - X_{10}}\right) \qquad (Eqn\ 3.4)$$

where, X and Y are coordinates of selected nodes.

After calculating the angle of attack, all nodes are rotated with the negative angle of attack value. By doing this, the airfoil is brought back to its zero angle of attack position. Then, the deformed airfoil is translated in such a way that the leading-edge node at deformed position has the same coordinates with its undeformed position. Finally, the deformation is recalculated by subtracting undeformed coordinates from rotated and translated deformed coordinates.

After calculating the final deformations for each selected node, an objective is defined for the optimization problem of targeting algorithm. The objective is defined using difference between the final deformation of NACA 0012 and NACA 2412 airfoil data coordinate difference. To calculate the difference between morphed airfoil and the target one, first, from both NACA0012 and NACA2412 airfoil coordinates, the nearest points to the selected nodes of the morphing airfoil model are taken. Then, the coordinate differences of the NACA0012 and NACA2412 are calculated for each selected point in order to calculate the deformation needed for

morphing. Each nodal difference between baseline airfoil and target one is denoted as $\delta\bar{X}_i$ and $\delta\bar{Y}_i$. Then, the objective for X and Y deformations are calculated using Equation 3.5 and Equation 3.6, respectively. At the end, the total objective is summation of X and Y objectives as seen in Equation 3.7.

$$Objective_X = 100 \times \sqrt{\sum_{j=1}^{20}\left(\delta\bar{X}_{ij} - \sum_{i=1}^{10}\delta X_{ij} kp_i\right)^2} \Big/ Chord\ Lengt \quad (Eqn\ 3.5)$$

$$Objective_Y = 100 \times \sqrt{\sum_{j=1}^{20}\left(\delta\bar{Y}_{ij} - \sum_{i=1}^{10}\delta Y_{ij} kp_i\right)^2} \Big/ Chord\ Lengt \quad (Eqn\ 3.6)$$

$$Objective_{XY} = Objective_X + Objective_Y \quad (Eqn\ 3.7)$$

In order to minimize the total objective ($Objective_{XY}$), the Microsoft® Excel Solver Tool is employed by using the GRG Non-linear (Generalized Reduced Gradient) method as the solving algorithm. By changing the *kp* values, the tool attempts to minimize the defined total objective. However, certain constraints are applied to the optimization problem in order to ensure the feasibility of the solution. Firstly, all pressure coefficient values are constrained to be positive, since negative pressure (i.e. vacuum) is not a viable option. Secondly, the $Objective_Y$ value is constrained to be less than 0.2. Since both baseline and target airfoil have chord of 500 mm, required morphing will be occurred in Y direction. This makes $Objective_Y$ more important parameter than $Objective_X$ in achieving a successful morphing. While the Solver tool is unable to find an $Objective_Y$ value smaller than 0.2 (i.e. 0.2 % of chord length), it does succeed in making $Objective_Y$ closer to 0.2.

Finally, it can be observed from Table 3.5 that the airfoil exhibits an angle of attack after pressurization. When the angle of attack value is constrained to 0, the Solver tool is unable to find a feasible solution due to the boundary conditions and the

working principles of the morphing airfoil. As a result, the angle of attack is not constrained to a specific value.

As a result of the calculations performed using the Microsoft® Excel Solver Tool, the *kp* values are determined and presented in Table 3.5. Additionally, the angle of attack, X and Y translation values of the leading-edge node, and the final objectives are tabulated in Table 3.5, providing a comprehensive summary of the results of the targeting algorithm.

Table 3.5 Output of the Targeting Algorithm

Actuator Pressures Coefficients									
***kp* Up1**	***kp* Up2**	***kp* Up3**	***kp* Up4**	***kp* Down1**	***kp* Down2**	***kp* Down3**	***kp* Down4**	***kp* Mid1**	***kp* Mid2**
0.134	0.630	0.000	0.142	0.058	0.000	0.015	0.000	0.008	0.000

Y Objective	**X Objective**	**XY Objective**	**Angle of Attack [degree]**	**Y Translation [mm]**	**X Translation [mm]**
0.274	4.129	4.397	3.323	-0.501	-0.711

3.5 Conclusion

In this chapter, the calculation of the targeting pressure distribution for the morphing airfoil is described. It is observed that by using an FE model (i.e. unit load model) and Microsoft® Excel, the pressure distribution necessary for morphing can be easily obtained. Moreover, once the Microsoft® Excel sheet is prepared, it can be used for different baseline and target airfoil combinations.

In this study, targeting pressure distribution is calculated for both NACA 0012 baseline and NACA 2412 target airfoils. It can be said that the calculated pressure distribution is in the range of applicable values. In conclusion, NACA 0012 to NACA 2412 airfoil morphing can be successfully achieved when the linear static FE analysis is taken into account.

CHAPTER 4

FINITE ELEMENT ANALYSIS OF THE MORPHING AIRFOIL

4.1 Introduction

In this chapter, the process of constructing both linear and non-linear finite element models of the morphing airfoil using the pressure distribution calculated with the targeting algorithm is described. The construction of the linear model is carried out first. Since the targeting algorithm assumes linear material behavior and small deflections, the results of the linear model are compared with those obtained from the targeting algorithm to validate their accuracy. Afterwards, the non-linear model of the designed airfoil is prepared using the same pressure distribution calculated with the targeting algorithm. The non-linear finite element analysis is then performed to determine the corrected pressure distribution from result steps of the non-linear FE model. Finally, using this final pressure multiplication factor, the non-linear analysis is repeated and the results are presented.

4.2 Geometric Linear Static Finite Element Analysis of Designed Airfoil Using Calculated Load Combination

The finite element model described in Chapter 3.2 is utilized to generate the geometric linear finite element model of the designed airfoil, as depicted in Figure 4.1. The pressure distribution provided in Table 4.1 is applied to the model, which is subject to the same constraints as outlined in Chapter 3.2. Specifically, the model is constrained with all translations and rotations at the middle line of the first spar, as shown in Figure 4.2. The analysis method selected for this purpose is linear static SOL101, which has been proven to be effective in predicting the deformation of the morphing airfoil under the applied pressure distribution.

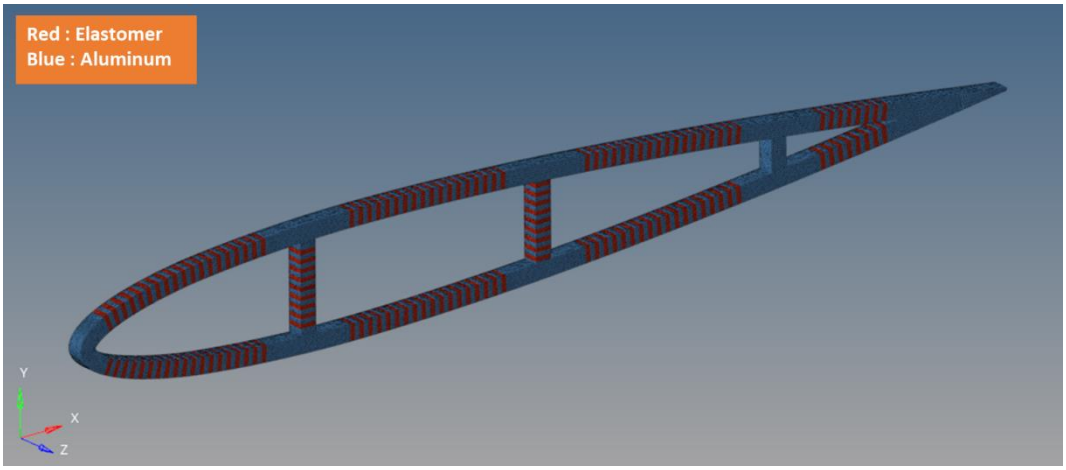

Figure 4.1. Finite Element Model of Designed Airfoil

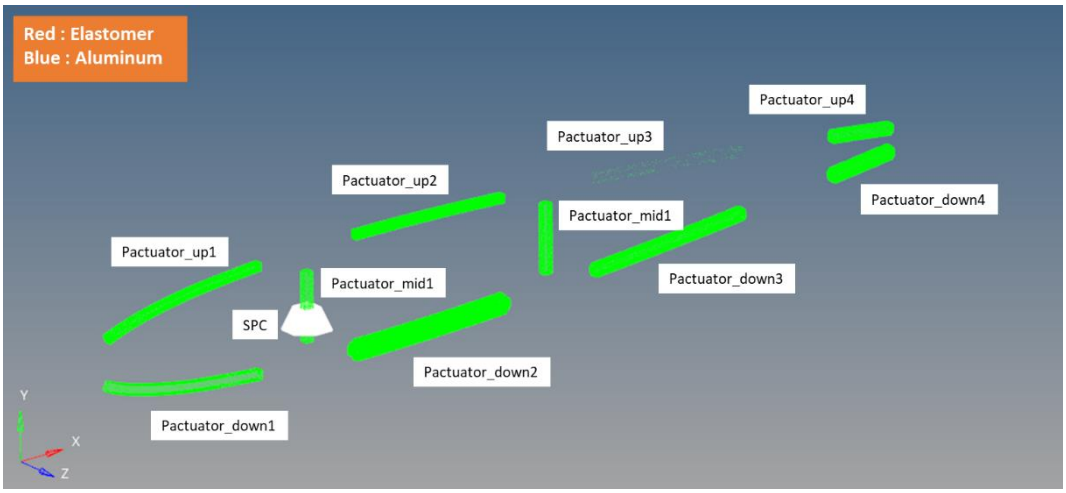

Figure 4.2. Loads and Boundary Conditions

Table 4.1 Pressure Distribution of the FE Model

Load Collectors Names	Pressure Value [MPa]
Pactuator_up1	0.134
Pactuator_up2	0.630
Pactuator_up3	0.000
Pactuator_up4	0.142
Pactuator_down1	0.058
Pactuator_down2	0.000
Pactuator_down3	0.015
Pactuator_down4	0.000
Pactuator_mid1	0.008
Pactuator_mid2	0.000

Before investigating the results of the linear static analysis, it is important to compare the targeting algorithm result with the linear static FE displacement result. This can be done by examining the difference between the final coordinates calculated via the targeting algorithm and the linear static FE results for selected nodes, as shown in Figure 3.4. The results of the comparison indicate that the final coordinates calculated with the targeting algorithm and the linear static FE analysis results are in close agreement as shown in Table 4.2. This suggests that it is possible to perform a linear static analysis externally using Microsoft® Excel and the unit load method.

Table 4.2 Targeting Algorithm- Linear FE Morphed Airfoil Result Comparison

Node ID	Targeting Algorithm		Linear Static FE Result		% Difference in X	% Difference in Y
	X Coordinate [mm]	Y Coordinate [mm]	X Coordinate [mm]	Y Coordinate [mm]		
1	479.38	-23.33	479.38	-23.26	0.0	0.3
2	440.59	-13.88	440.59	-13.82	0.0	0.4
3	395.80	-4.21	395.80	-4.17	0.0	1.1
4	364.39	1.92	364.38	1.96	0.0	-2.0
5	272.78	17.95	272.78	17.96	0.0	-0.1
6	236.34	23.33	236.34	23.34	0.0	0.0
7	139.13	29.85	139.13	29.85	0.0	0.0
8	98.22	28.52	98.22	28.52	0.0	0.0
9	9.71	11.73	9.71	11.72	0.0	0.1
10	-0.71	-0.50	-0.71	-0.51	0.2	-1.6
11	10.01	-12.47	10.01	-12.48	0.0	-0.1
12	98.12	-28.28	98.12	-28.29	0.0	0.0
13	138.99	-30.01	138.99	-30.01	0.0	0.0
14	231.44	-31.67	231.45	-31.66	0.0	0.0
15	268.27	-32.54	268.27	-32.53	0.0	0.0
16	361.35	-32.54	361.36	-32.50	0.0	0.1
17	393.35	-31.99	393.36	-31.94	0.0	0.1
18	438.62	-31.36	438.62	-31.31	0.0	0.2
19	478.54	-30.79	478.54	-30.72	0.0	0.2
20	502.50	-29.72	502.50	-29.64	0.0	0.2

The analysis results are presented first, in terms of the deformations, then, in terms of the strain values of the elastomeric chamber of the actuator and the stress values of the aluminum stiffeners; and finally, in terms of the stress values of the rest of the aluminum region which does not have any actuators.

Figure 4.3 illustrates the deformation of the designed morphing airfoil under pressure distribution calculated by using the targeting algorithm. As shown in the figure, the designed airfoil morphs into the target airfoil NACA2412 from the starting airfoil NACA0012.

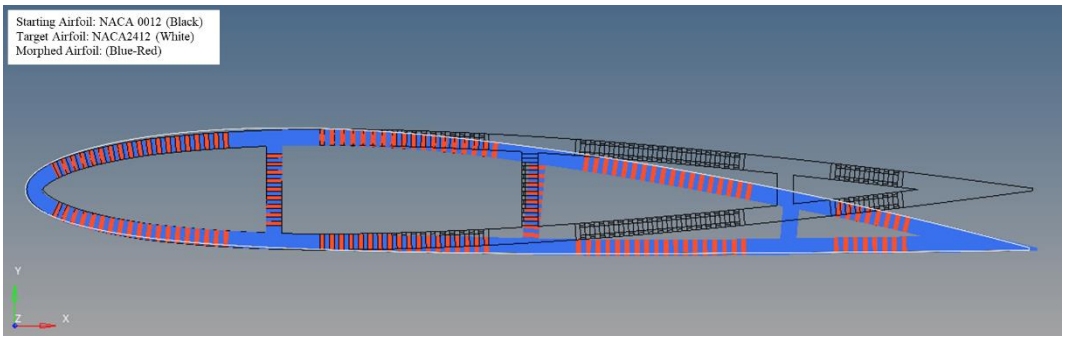

Figure 4.3. Linear FE Analysis Deformation of the Designed Airfoil

Upon closer examination, it can be seen that the coordinate difference at the leading edge is almost zero (Figure 4.4). However, as shown in Figure 4.4, there is a coordinate difference between the morphed airfoil and the target airfoil from the leading edge to the first spar location, in other words, the lines representing the morphed airfoil and the target airfoil do not exactly overlap. The upper part of the airfoil is unable to reach the target line, while the lower part surpasses it. This is due to the constraint at the midline of the first spar which allows the actuator at this location to deform but not translate or rotate. As a result, it is observed from the minimization process that the biggest portion of the objective is linked to the fact that the region corresponding to the maximum thickness does not exactly match with the target airfoil line.

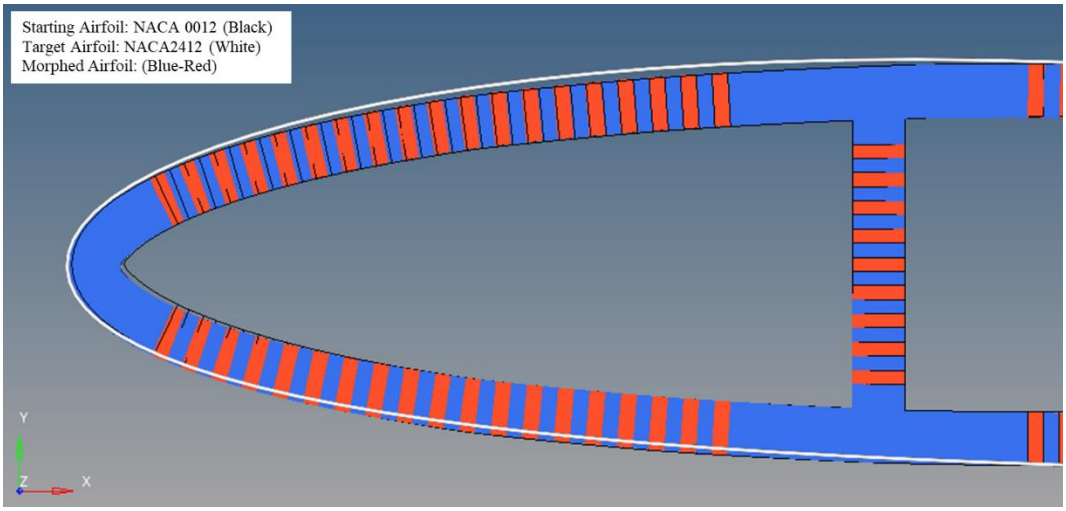

Figure 4.4. Deformation at the Leading Edge Region

A detailed analysis of the region between the first and the third spar, as depicted in Figure 4.5, reveals that there is a relatively smaller coordinate difference between the morphed airfoil and the target airfoil. This can be attributed to the fact that the second spar is not constrained and has the ability to both rotate and translate which enables more successful morphing results in this region. This also demonstrates the importance of having adequate degrees of freedom in the morphing process in order to achieve the desired shape transformation.

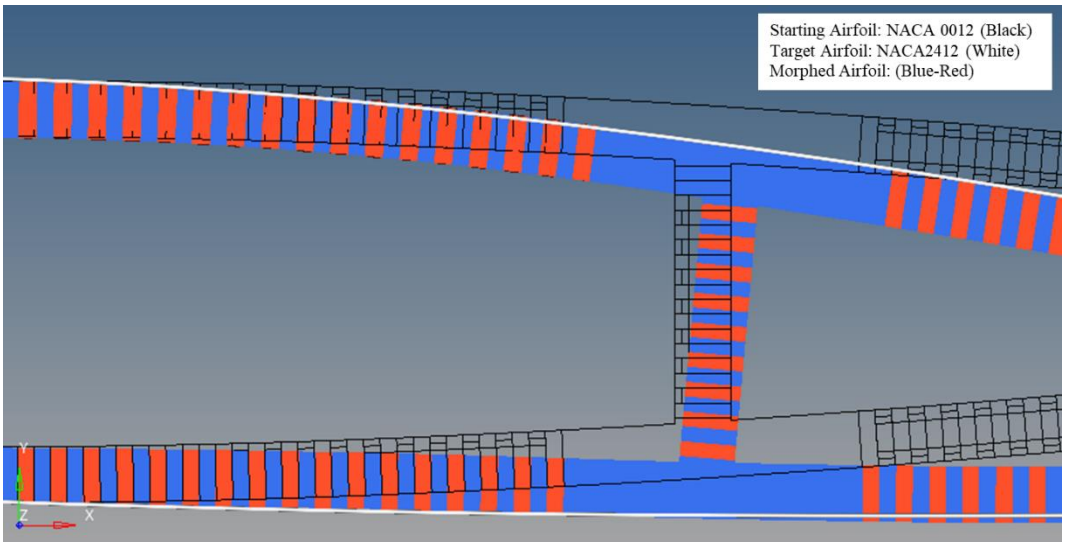

Figure 4.5. Deformation at the Middle Region

As depicted in Figure 4.6, an examination of the region between the third spar and the trailing edge reveals that there are some coordinate differences between the morphed airfoil and the target airfoil. However, upon closer inspection at the trailing edge, it can be observed that the coordinate difference in the Y direction becomes zero. The trailing edge of the morphed airfoil aligns perfectly with the target airfoil trailing edge by also demonstrating the effectiveness of the targeting algorithm in achieving the desired shape transformation.

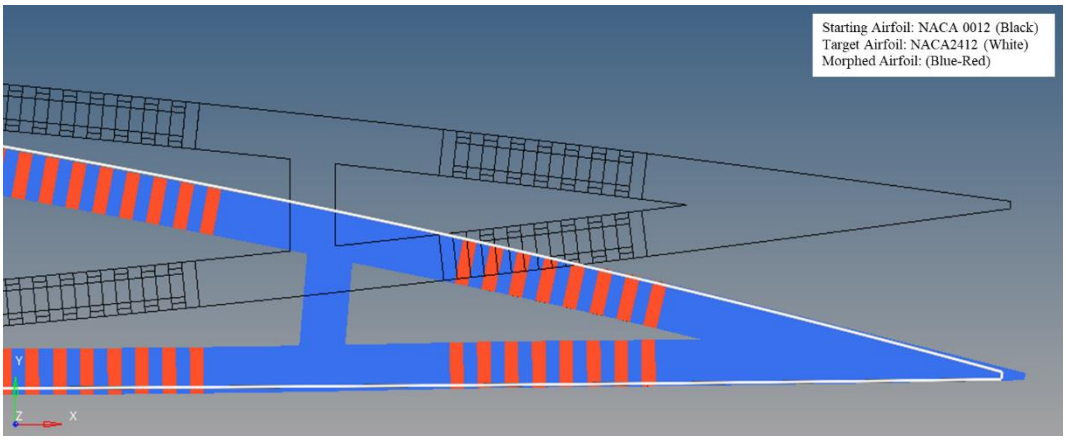

Figure 4.6. Deformation at the Trailing Edge Region

An examination of the overall shape transformation reveals that the leading edge and the trailing edge of the morphed airfoil are able to accurately match the target airfoil with the NACA 2412 profile. However, between the leading edge and the trailing edge, some coordinate differences are observed and this is due to the constraint imposed at the middle line of the first spar actuator limiting the ability of the morphing process to fully achieve the desired shape transformation in this region. Despite this limitation, the targeting algorithm is able to effectively achieve the overall desired shape transformation with a high degree of accuracy.

Upon investigation of the strain results, it is observed that the maximum strain value occurs at the elastomer region of the Up2 actuator. As depicted in Figure 4.7 and Figure 4.8, the elastomer region of the Up2 actuator exhibits a strain value of 0.21808. This strain value falls within the failure threshold of the elastomeric material indicating that it is able to withstand the applied loads. The strain values of the rest of the elastomeric chamber are summarized in Table 4.3.

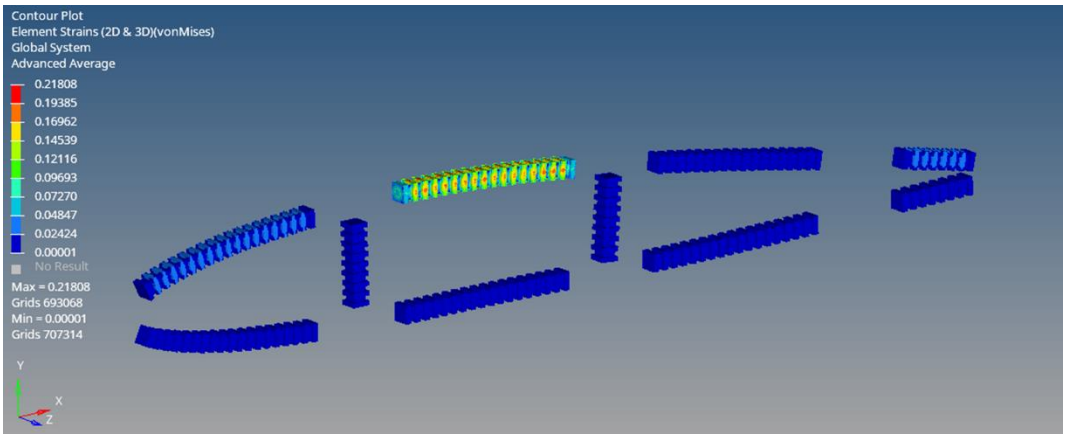

Figure 4.7. Von-Mises Strain Result of Elastomeric Chamber of Cell Actuators.

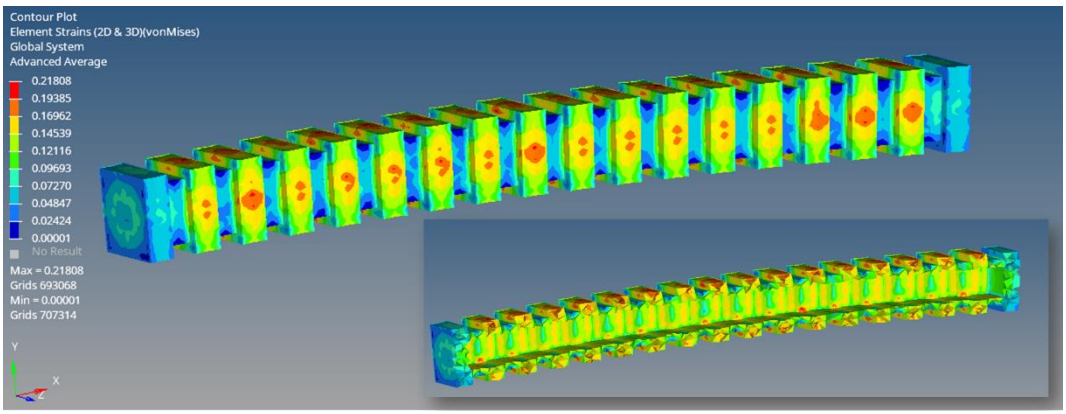

Figure 4.8. Von-Mises Strain Result of Elastomeric Chamber of Up2 Actuators

Following the investigation of the strain values of the elastomeric region, the Von-Mises stress values of the aluminum stiffener region are also examined. It is found that the maximum stress value occurs at the Up2 actuator region, as shown in Figure 4.9 and Figure 4.10. The stress value at this location is 27.4 MPa indicating the high loads being applied to this region.

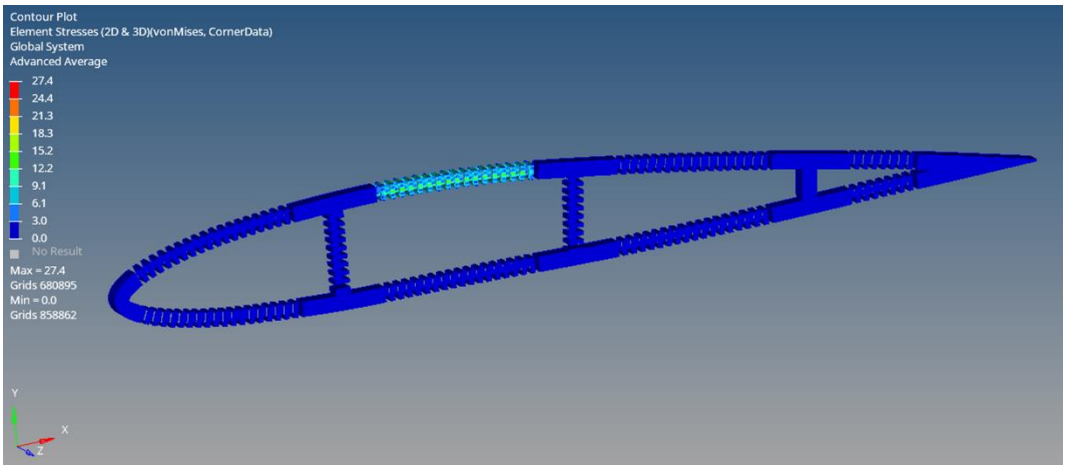

Figure 4.9. Von-Mises Stress Result of Aluminum Region of the Morphing Airfoil.

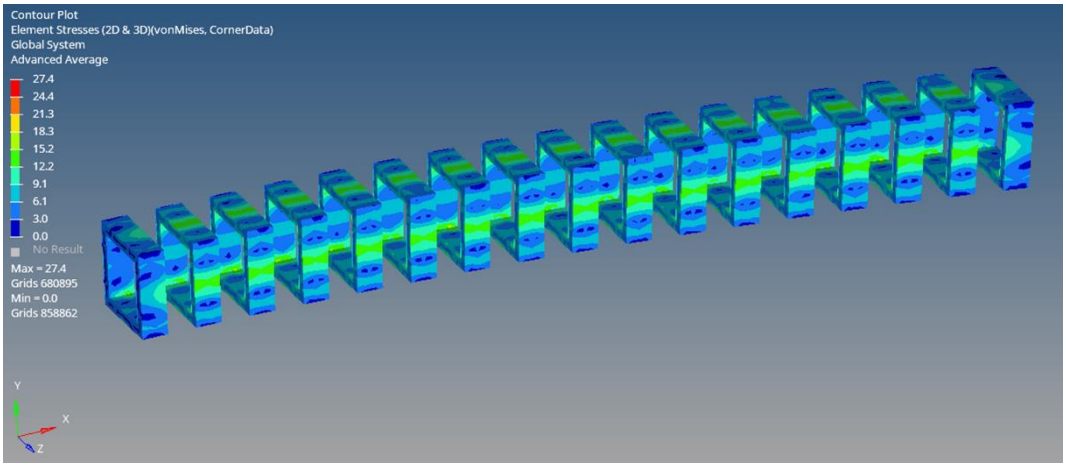

Figure 4.10. Von-Mises Stress Result of Aluminum Stiffener of Up2 Actuator

Upon examination of Figure 4.10, it becomes evident that the maximum stress region is not visible. The maximum stress is located at a single point, which makes it difficult to accurately assess the stress distribution in the Up2 actuator aluminum stiffener region. In order to obtain clear understanding of the actual stress distribution, a filter is applied to the stress plot such that only the stress values smaller than 27 MPa are plotted. The resulting stress distribution is shown in Figure 4.11, which reveals the maximum stress region. The application of the filter results in a decrease of the maximum Von-Mises value to 19.2 MPa which is a much lower value

than aluminum yield strength (larger than 200 MPa for aerospace aluminums). The stress values of the rest of the aluminum stiffeners are summarized in Table 4.3.

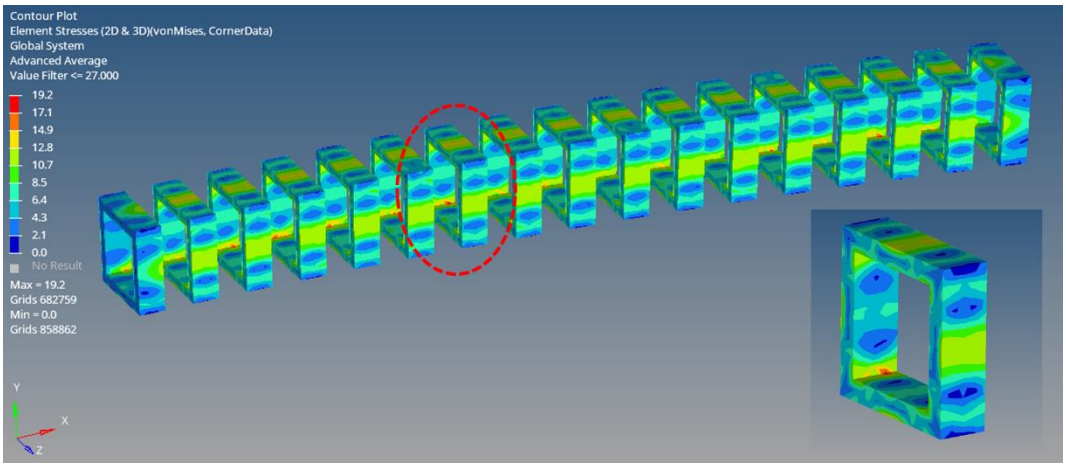

Figure 4.11. Von-Mises Stress Result of Aluminum Stiffener of Up2 Actuator (Filtered)

Table 4.3 Strain and Stress Results of Actuators

Actuator Name	Elastomeric Chamber Von-Mises Strain [mm/mm]	Aluminum Stiffener Von-Mises Stress [MPa]
Up1	0.04696	4.04
Up2	0.21808	27.40
Up3	0.00084	0.02
Up4	0.04989	4.00
Down1	0.02257	1.96
Down2	0.01122	0.22
Down3	0.00569	0.43
Down4	0.01013	0.17
Mid1	0.00657	0.28
Mid2	0.00685	0.12

The areas where actuators are not present exhibit low Von-Mises stress values, as demonstrated in Figure 4.12. The maximum Von-Mises stress value in these regions is 0.8 MPa. It is also worth noting that the maximum stress of the aluminum parts where there are no actuators occurs at the end of the Up2 actuator, indicating the influence of the actuator on the stress distribution in the surrounding aluminum structure.

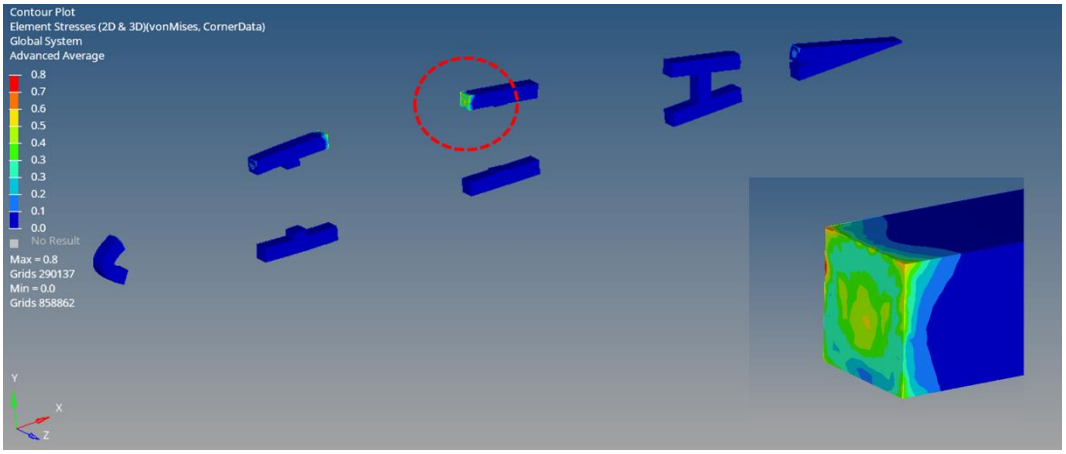

Figure 4.12. Von-Mises Stress Result of Region where no Actuators are placed

4.3 Geometric Non-Linear Static Finite Element Analysis of Designed Airfoil Using Calculated Load Combination

In this section, the non-linear static analysis of the morphing airfoil is conducted after completing the linear static analysis. For small deformations, the linear FE modelling and analysis is sufficient and the unit load method provides accurate results. However, for larger deformations, a non-linear modelling and analysis is required.

The pressure distribution presented in Table 4.1, which has been calculated by using a targeting algorithm, is utilized in the same manner as it was in the linear static FE analysis. The non-linear analysis is carried out using 10 load sub-increments, meaning that the load is increased by 0.1 at each step. In addition, by using a "follower force" [27], the pressure vectors are recalculated at each load increment and applied perpendicularly to the inner surface of the elastomeric chamber.

As shown in Figure 4.13, the non-linear static FE analysis of the morphing airfoil at load levels of 0% and 100% is depicted. It is evident from the figure that the solution is over-shoot at a load level of 100%. The comparison of the load levels of 70.9% and 82.4% shown in Figure 4.14 reveals that the optimal solution is likely to be achieved at a load level of 75%.

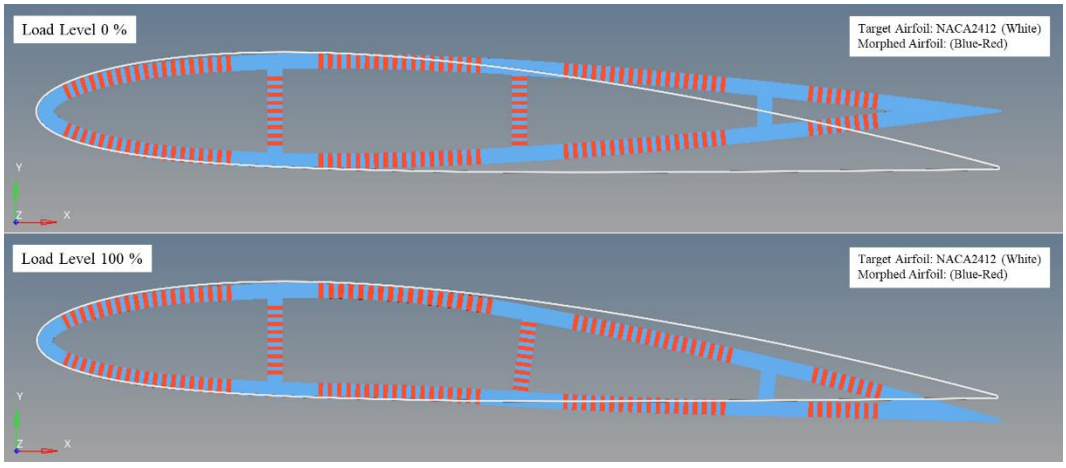

Figure 4.13. Non-linear FE Result at Load Level 0 % and 100 %

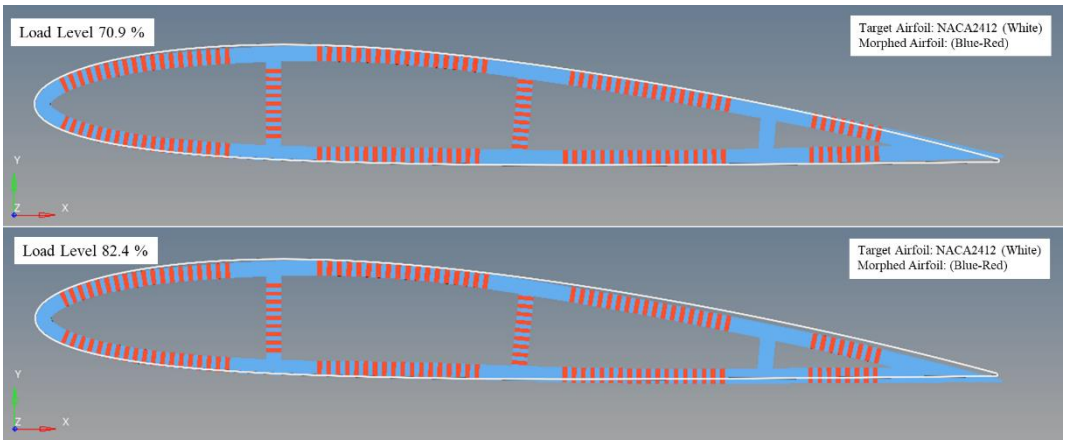

Figure 4.14. Non-linear FE Result at Load Level 70.9 % and 82.4 %

In order to obtain improved morphing results, the pressure distribution is multiplied by a factor of 0.75, which is the pressure multiplication factor for the NACA 0012 to NACA2412 morphing case. The non-linear FE analysis is then repeated with 5 load sub-increments. In Figure 4.15, the results of the finite element analysis of the morphing airfoil with the modified pressure distribution which is multiplied by 0.75 is presented. This new pressure distribution is referred to as the "modified pressure distribution" and is outlined in Table 4.4.

Table 4.4 Modified Pressure Distribution

Load Collectors Names	Pressure Value [MPa]
Pactuator_up1	0.100
Pactuator_up2	0.473
Pactuator_up3	0.000
Pactuator_up4	0.106
Pactuator_down1	0.044
Pactuator_down2	0.000
Pactuator_down3	0.011
Pactuator_down4	0.000
Pactuator_mid1	0.006
Pactuator_mid2	0.000

Non-linear analysis completed with total number of 36 load increments and 138 iterations in 10 hours. For better convergence, Altair® OptiStruct solver increases the load increment from 10 to 36. The detailed non-linear convergence histories are presented in Appendix B.

As in linear FE analysis, the results of the non-linear analysis are presented first in terms of deformation and then in terms of the strain values of the elastomeric chamber of the actuator and the stress values of the aluminum stiffeners. Finally, the stress values of the remaining aluminum region that does not include any actuator are presented.

Figure 4.15 illustrates the deformation of the designed morphing airfoil under the modified pressure distribution. As depicted in the figure, the designed airfoil morphs into the target airfoil NACA 2412 from the starting airfoil NACA 0012.

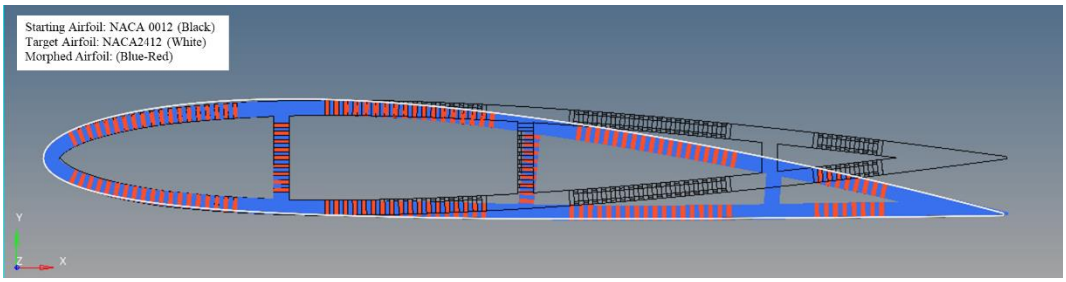

Figure 4.15. Non-Linear FE Analysis Deformation of the Designed Airfoil

Upon further examination of the non-linear deformation, it becomes apparent that, in concurrence with the results of the linear FE analysis, there exists a slight deviation in the coordinates between the transformed airfoil and the target airfoil, specifically in the region extending from the leading edge to the first spar, as compared to the rest of the airfoil. This deviation can be easily discerned upon closer examination of Figure 4.16, Figure 4.17, and Figure 4.18. As previously discussed in the chapter pertaining to linear FE analysis, it is noted that the objective at the boundary condition region, specifically the first spar, is significantly higher in comparison to other regions of the airfoil.

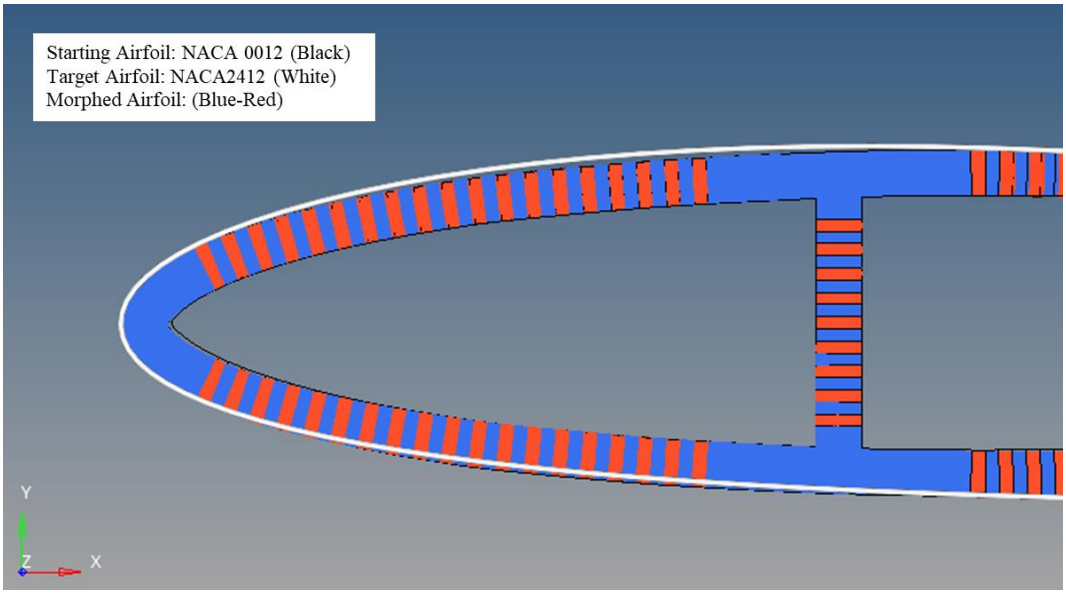

Figure 4.16. Deformation at the Leading Edge Region (Non-Linear Model)

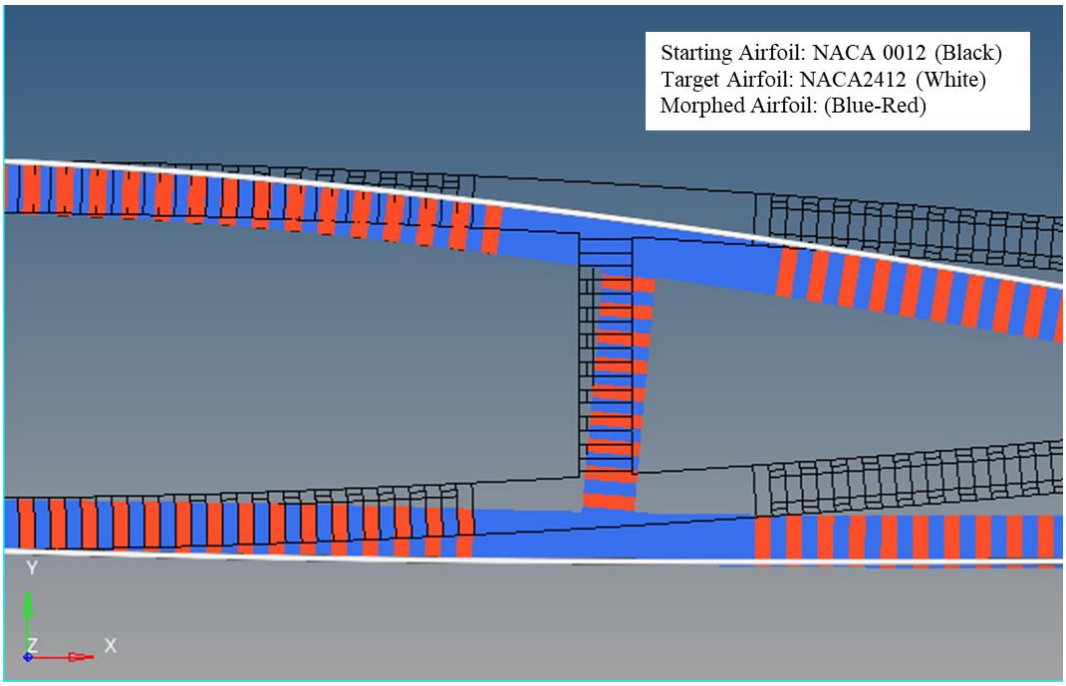

Figure 4.17. Deformation at the Middle Region (Non-Linear Model)

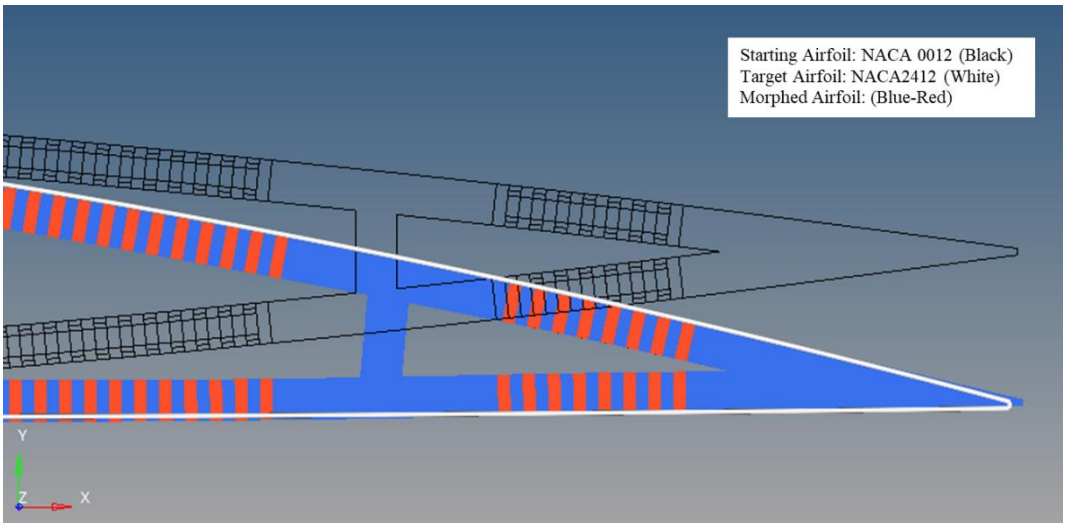

Figure 4.18. Deformation at the Trailing Edge Region (Non-Linear Model)

The overall morphing process demonstrates that the leading edge and the trailing edge of the airfoil are able to match the targeted NACA 2412 airfoil with a high degree of success. However, it is observed that there is a slight deviation in the coordinates between the morphed airfoil and the target airfoil in the region between the leading edge and the trailing edge.

Subsequently, the strain results of the elastomeric region of the actuators are analyzed. The results reveal that the maximum strain values are observed at the Up2 actuator region. As depicted in Figure 4.19 and 4.20, the elastomeric chamber of the Up2 actuator exhibits a strain value of 0.21037. It is worth noting that this strain value is below the ultimate strength of the elastomeric material employed. The remaining maximum strain values for each actuator are presented in Table 4.5.

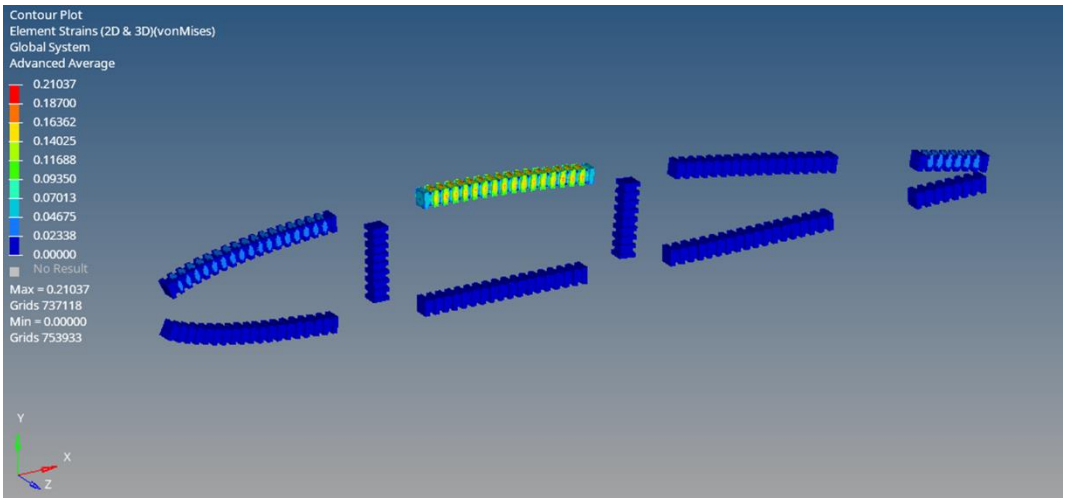

Figure 4.19. Von-Mises Strain Result of Elastomeric Chamber of Cell Actuators.

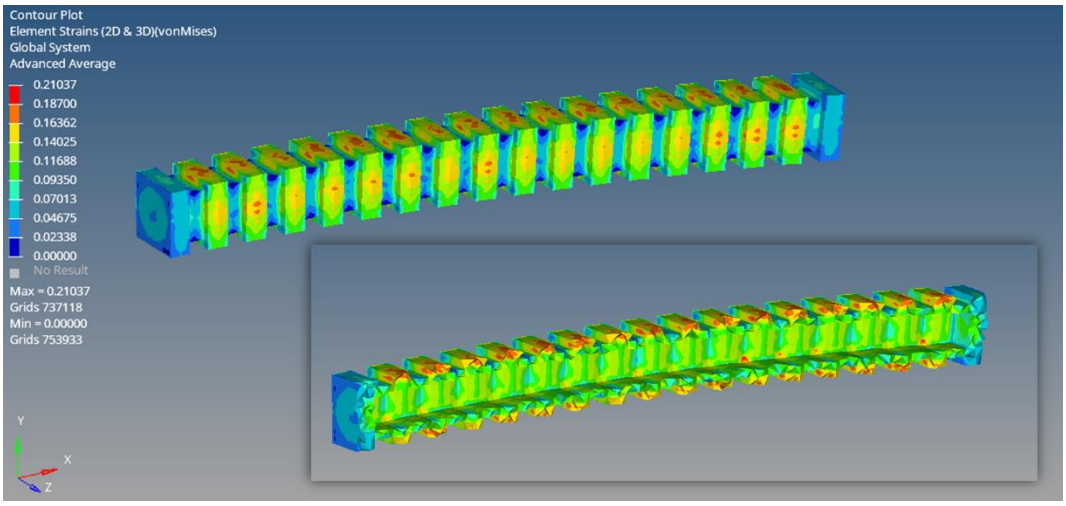

Figure 4.20. Von-Mises Strain Result of Elastomeric Chamber of Up2 Actuators

Following the examination of the strain values of the elastomeric region, the investigation proceeds to the analysis of the Von-Mises stress values of the aluminum stiffener region. As expected, the maximum stress value is observed at the Up2 actuator region. As illustrated in Figure 4.21 and 4.22, the highest stress value at this region is 22.4 MPa, which corresponds to the application of maximum pressure on the Up2 actuator.

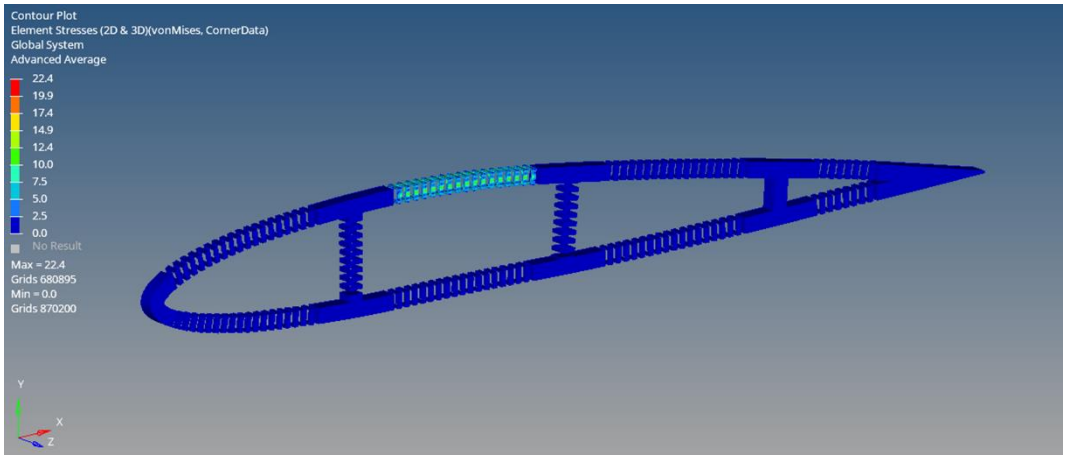

Figure 4.21. Von-Mises Stress Result of Aluminum Region of the Morphing Airfoil.

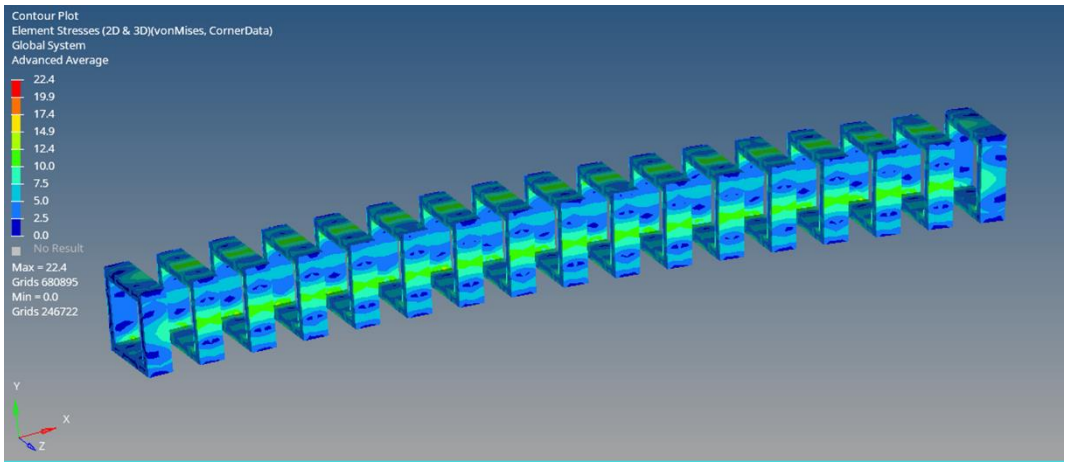

Figure 4.22. Von-Mises Stress Result of Aluminum Stiffener of Up2 Actuator

Upon examination of Figure 4.22, it can be observed that the maximum stress region is not clearly visible. The maximum stress is concentrated at a single point, which makes it challenging to accurately determine the stress distribution. In order to gain a clearer understanding of the stress distribution of the Up2 actuator aluminum stiffener region, a filter is applied to the stress plot such that only stress values smaller than 22 MPa are plotted. The resulting stress distribution is depicted in Figure 4.23. From this figure, it is possible to discern the maximum stress region with a greater precision. After filtering the stress values, the maximum Von-Mises value dropped to 15.7 MPa which is significantly lower than the aluminum yield strength (for aerospace aluminums, the value is typically greater than 200 MPa). The stress values of the remaining aluminum stiffeners are presented in Table 4.5.

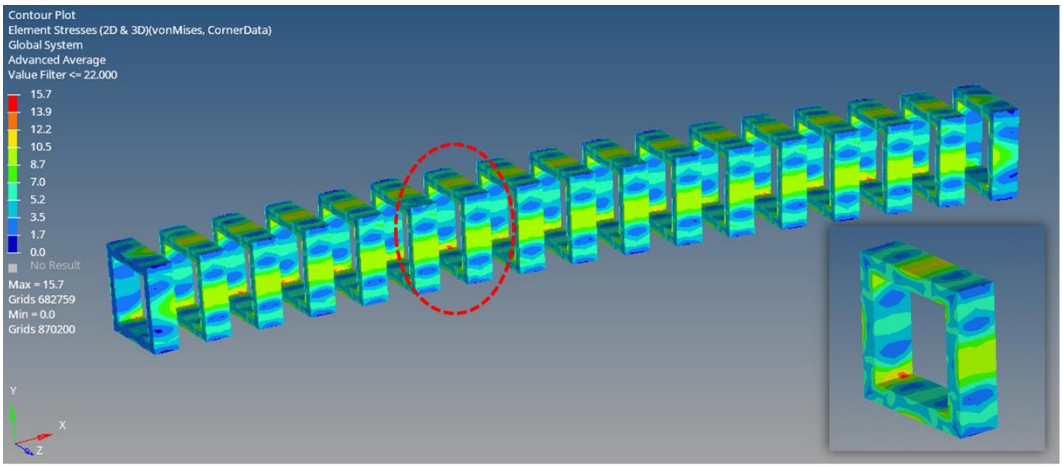

Figure 4.23. Von-Mises Stress Result of Aluminum Stiffener of Up2 Actuator (Filtered)

Table 4.5 Strain and Stress Results of Actuators

Actuator Name	Elastomeric Chamber Von-Mises Strain [mm/mm]	Aluminum Stiffener Von-Mises Stress [MPa]
Up1	0.03968	3.09
Up2	0.21037	22.40
Up3	0.00038	0.005
Up4	0.04402	3.06
Down1	0.01823	1.50
Down2	0.01059	0.14
Down3	0.00477	0.33
Down4	0.00861	0.12
Mid1	0.00541	0.22
Mid2	0.00543	0.09

The regions where no actuators are located exhibit low Von-Mises stress values, as depicted in Figure 4.24. The maximum Von-Mises stress value for this region is found to be 0.5 MPa. It can be noted that the maximum stress of the aluminum parts where there is no actuator occurs at the end of the Up2 actuator.

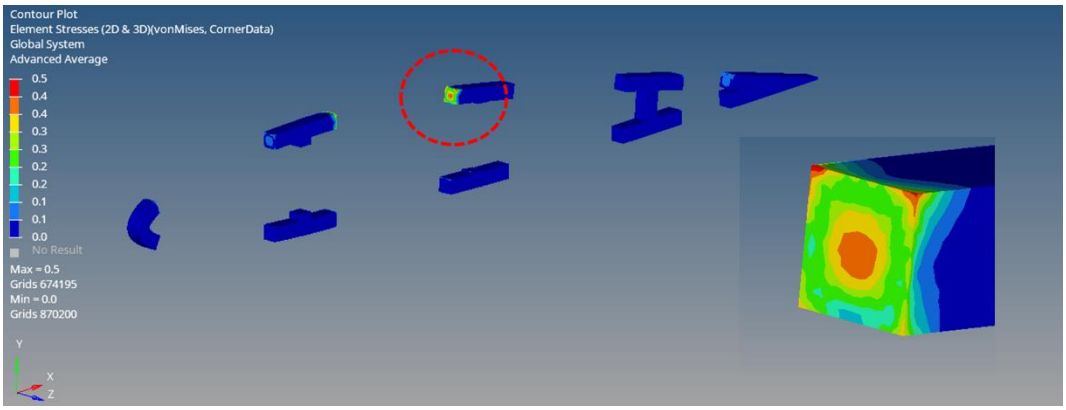

Figure 4.24. Von-Mises Stress Result of Parts where no Actuators are placed

4.4 Conclusion

After both linear and non-linear FE analysis results are presented, a comparison of the results is conducted. Both linear and non-linear FE models utilize the same sizing data for all components. Furthermore, the material used, mesh size, element type, and boundary conditions are also identical for each model. The only distinction between the two models is the pressure distribution applied to the cell actuators. For the linear FE model, the pressure distribution calculated via the targeting algorithm is applied directly. However, for the non-linear FE model, the pressure distribution calculated by using the targeting algorithm is multiplied by 0.75 in order to achieve a similar level of successful morphing performance as the linear FE model.

In order to comprehend the difference between the linear and non-linear models and analyses, the displacement results for both cases are first presented in Figure 4.25, and then the results of both analyses are tabulated in Table 4.6 and 4.7 in terms of strain and stress.

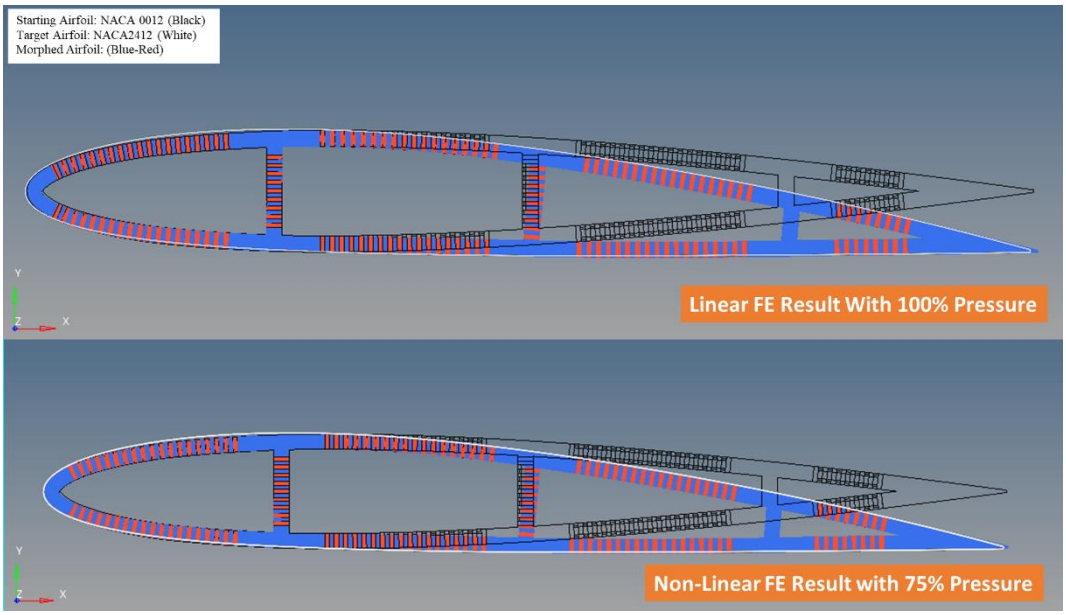

Figure 4.25. Linear and Non-Linear Deformation Results

Table 4.6 Linear and Non-Linear Model Strain Comparison

Actuator Name	Elastomeric Chamber Von-Mises Strain [mm/mm] Linear	Elastomeric Chamber Von-Mises Strain [mm/mm] Non-Linear	% Difference
Up1	0.04696	0.03968	-15.5
Up2	0.21808	0.21037	-3.5
Up3	0.00084	0.00038	-54.8
Up4	0.04989	0.04402	-11.8
Down1	0.02257	0.01823	-19.2
Down2	0.01122	0.01059	-5.6
Down3	0.00569	0.00477	-16.2
Down4	0.01013	0.00861	-15.0
Mid1	0.00657	0.00541	-17.7
Mid2	0.00685	0.00543	-20.7

Table 4.7 Linear and Non-Linear Model Stress Comparison

Actuator Name	Aluminum Stiffener Von-Mises Stress [MPa] Linear	Aluminum Stiffener Von-Mises Stress [MPa] Non-Linear	% Difference
Up1	4.04	3.09	-23.5
Up2	27.40	22.40	-18.2
Up3	0.02	0.005	-75.0
Up4	4.00	3.06	-23.5
Down1	1.96	1.50	-23.5
Down2	0.22	0.14	-36.4
Down3	0.43	0.33	-23.3
Down4	0.17	0.12	-29.4
Mid1	0.28	0.22	-21.4
Mid2	0.12	0.09	-25.0

From the data presented in Table 4.6 and 4.7, it can be inferred that both the stress and strain values are lower in the non-linear analysis. This outcome is expected, as the applied pressure distribution for the non-linear model is 25% less than that of the linear model. This reduction in pressure results in lower stress and strain values.

CHAPTER 5

CONCLUSION

5.1 General Conclusions

The main objective of this thesis is to design a pressure-driven morphing airfoil capable of morphing from a baseline airfoil (NACA0012) to a target one (NACA2412) via cell actuators by using a targeting algorithm that calculates the cell actuator pressure distribution.

A pressure-driven morphing airfoil design, finite element modeling and analysis are presented in this thesis. It is shown that with the help of a targeting algorithm, a baseline airfoil design can morph into a target airfoil profile having different lift and drag coefficients.

As a conclusion, the implementation of a morphing airfoil design in the construction of aircraft and wind turbine blades has the potential to significantly enhance mission capabilities while also increasing the overall efficiency of the air vehicle. Furthermore, by utilizing this advanced design, wind turbine blades will have the ability to operate effectively in a wider range of weather conditions, thereby improving their overall performance and reliability. On the other hand, the integration of a specialized targeting algorithm into the design of a morphing airfoil can greatly simplify the process of calculating the pressure distribution that is necessary for the successful implementation of this advanced technology. By using this targeting algorithm, it is only necessary to perform a single calculation, in combination with a non-linear FE analysis, in order to accurately determine the pressure distribution of the morphing airfoil and achieve the desired target airfoil shape.

5.2 Recommendation for Future Work

This structural analysis study can also be performed by using different material combinations. Additionally, system can be optimized to obtain much lower actuator pressure values through different cell actuator dimensions and locations.

Material modeling can be improved and for the hyperelastic material modeling, more advanced material models, such as Mooney-Rivlin or Marlov, can be used instead of Neo-Hookean.

Cell actuator geometries can be optimized in order to provide much more efficient morphing action under lower pressure levels.

The utilization of this morphing airfoil design enables the development of a complete morphing wing, capable of adapting to a variety of different flight conditions. Furthermore, this type of morphing design can also be implemented as a control surface, allowing for precise adjustments to be made during operation. Additionally, this technology can also be utilized to create wings that can twist during operation, providing an additional level of control and versatility.

Since the wing of an aircraft is subjected to cyclic loading, for a morphing wing design using this morphing airfoil, fatigue and damage tolerance analysis can also be performed.

The results of this study can be evaluated and compared against the performance of a morphing airfoil that has been manufactured and subjected to testing, providing valuable insight into the accuracy and effectiveness of the analysis methods that were employed. This process of comparing the analysis results with the ones obtained through a physical testing could help to identify discrepancies and areas requiring improvement. The proposed approach can ultimately be used to further refine the design of the morphing airfoil in order to maximize its efficiency and performance.

REFERENCES

[1] S. Barbarino, O. Bilgen, R. M. Ajaj, M. I. Friswell, and D. J. Inman, "A Review of Morphing Aircraft," *Journal of Intelligent Material Systems and Structures*, vol. 22, no. 9. pp. 823–877, Jun. 2011.

[2] U. Kalkan, "Aero-Structural Analysis Of The Morphing Trailing Edge Control Surface Of A Fully Morphing Unmanned Aerial Vehicle Wing", Thesis, Middle East Technical University, 2017.

[3] D. S. Korpe, "Aerodynamic Modelling and Optimization of Morphing Wings", Thesis, Middle East Technical University, 2014.

[4] D. S. Korpe and S. Ozgen, "Morphing Wing Optimization for Steady Level Flight," *Proc Inst Mech Eng G J Aerosp Eng*, vol. 231, no. 13, pp. 2317–2330, Nov. 2017.

[5] P. L. Bishay and C. Aguilar, "Parametric Study of a Composite Skin for a Twist-Morphing Wing," *Aerospace*, vol. 8, no. 9, Sep. 2021.

[6] H. L. Sahin, "Synthesis, Analysis And Design Of A Novel Mechanism For The Trailing Edge Of A Morphing Wing", Thesis, Middle East Technical University, 2018.

[7] I. O. Tunçöz, Y. Yang, E. Gürses, M. Sahin, S. Özgen and Y. Yaman, "A Hybrid Trailing Edge Control Surface Capable of Camber and Decamber Morphing", SMART2015, 7 th ECCOMAS Thematic Conference on Smart Structures and Materials, 03-06 June 2015, Ponta Delgada, Azores, Portugal

[8] P. Arslan, U. Kalkan, H. Tiras, I. O. Tuncoz, Y. Yang, E. Gurses, M. Sahin, S. Ozgen, Y. Yaman, "A Hybrid Trailing Edge Control Surface Concept", DeMEASS-VI, 6 th Conference for Design, Modelling and Experiments of Advanced Structures and Systems, 25-28 May 2014, Ede-Wageningen, Netherlands

[9] I. O. Tuncoz, Y. Yang, E. Gürses, M. Sahin, S. Ozgen and Y. Yaman, "Hybrid Morphing Trailing Edge Designed for Camber Change of the Control Surface", SciTech 2016, AIAA Science and Technology Forum 2016, 04-08 January 2016, San Diego, USA, AIAA-2016-0316.

[10] P. Arslan, U. Kalkan, H. Tiras, I. O. Tuncoz, Y. Yang, E. Gurses, M. Sahin, S. Ozgen, and Y. Yaman, "Structural Analysis of an Unconventional Hybrid Control Surface of a Morphing Wing", ICAST2014: 25 th International Conference on Adaptive Structures and Technologies, 06-08 October 2014, The Hague, Netherlands.

[11] E. Gurses, I. O. Tuncoz, Y. Yang, P. Arslan, U. Kalkan, H. Tiras, M. Sahin, S. Ozgen and Y. Yaman, "Structural and Aerodynamic Analyses of a Hybrid Trailing Edge Control Surface of a Fully Morphing Wing", Journal of Intelligent Material Systems and Structures, 28(8), 979-991 (2017)

[12] I. O. Tuncoz, Y. Yang, E. Gürses, M. Sahin, S. Ozgen, and Y. Yaman, "A Hybrid Trailing Edge Control Surface Capable of Camber and Decamber Morphing", SMART2015, 7 th ECCOMAS Thematic Conference on Smart Structures and Materials, 03-06 June 2015, Ponta Delgada, Azores, Portugal

[13] J. Sun, Q. Guan, Y. Liu, and J. Leng, "Morphing Aircraft Based on Smart Materials and Structures," *Journal of Intelligent Material Systems and Structures*, vol. 27, no. 17. SAGE Publications Ltd, pp. 2289–2312, 2016.

[14] I. Dayyani, A. D. Shaw, E. I. Saavedra Flores, and M. I. Friswell, "The Mechanics of Composite Corrugated Structures" *Composite Structures*, vol. 133. Elsevier Ltd, pp. 358–380, Dec. 01, 2015.

[15] S. Vasista and L. Tong, "Topology-Optimized Design and Testing of a Pressure-Driven Morphing-Aerofoil Trailing-Edge Structure," *AIAA Journal*, vol. 51, no. 8, pp. 1898–1907, Aug. 2013.

[16] S. Vasista and L. Tong, “Pressurized Morphing Wing Structures,” *AIAA/ASME/ASCE/AHS/ASC Structures, Structural Dynamics and Materials Conference*, 2012.

[17] S. Vasista, L. Tong, and K. C. Wong, “Realization of Morphing Wings: A Multidisciplinary Challenge,” *J Aircr*, vol. 49, no. 1, pp. 11–28, 2012.

[18] S. Vasista, J. Riemenschneider, T. Mendrock, and H. P. Monner, “Pressure Driven Morphing Devices For 3d Shape Changes With Multiple Degrees Of Freedom,” SMASIS2018-7949, 2018.

[19] S. Vasista, J. Riemenschneider, R. Keimer, H. P. Monner, F. Nolte, and P. Horst, “Morphing Wing Droop Nose With Large Deformation: Ground Tests and Lessons Learned,” *Aerospace*, vol. 6, no. 10, pp. 1–21, 2019.

[20] S. Vasista, M. Titze, M. Schäfer, O. Bertram, J. Riemenschneider, and H. P. Monner, “Structural and Systems Modeling of a Fluid-Driven Morphing Winglet Trailing Edge,” in *AIAA Scitech 2020 Forum*, 2020, vol. 1 PartF, pp. 1–19

[21] S. Vasista, K. Büchner, M. Titze, J. Riemenschneider, H. P. Monner, and V. Seitz, “Modeling and Experiments of Additively-Manufactured Fluid Actuated Morphing Unit Structures” ACTUATOR; International Conference and Exhibition on New Actuator Systems and Applications, 2021, pp. 1-6.

[22] S. Vasista, A. de Gaspari, S. Ricci, J. Riemenschneider, H. P. Monner, and B. van de Kamp, “Compliant Structures-Based Wing and Wingtip Morphing Devices,” *Aircraft Engineering and Aerospace Technology*, vol. 88, no. 2, pp. 311–330, Mar. 2016,

[23] S. Vasista and L. Tong, “Design and Testing of Pressurized Cellular Planar Morphing Structures,” *AIAA Journal*, vol. 50, no. 6, pp. 1328–1338, Jun. 2012.

[24] T. L. Vasista S., “Design Considerations Of A Pressure Driven Morphing Wing Structure,” 28th Congress of the International Council of the Aeronautical Sciences 2012, ICAS 2012. 3. 2174-2183.

[25] S. Paulo, “The Airfoil Thickness Effects on Wavy Leading Edge Phenomena at Low Reynolds Number Regime,”, Thesis, University of Sao Paulo, 2016.

[26] Q. Zhang, X. Li, and Q. Yang, “Extracting the Isotropic Uniaxial Stress-Strain Relationship of Hyperelastic Soft Materials Based on New Nonlinear Indentation Strain and Stress Measure,” *AIP Adv*, vol. 8, no. 11, Nov. 2018.

[27] A. K. Jha and D. J. Inman, “Importance of Geometric Non-Linearity and Follower Pressure Load in the Dynamic Analysis of a Gossamer Structure,” *J Sound Vib*, vol. 278, no. 1–2, pp. 207–231, Nov. 2004.

APPENDICES

APPENDIX A

Mesh Size Comparison – Deformations Under Unit Load Cases

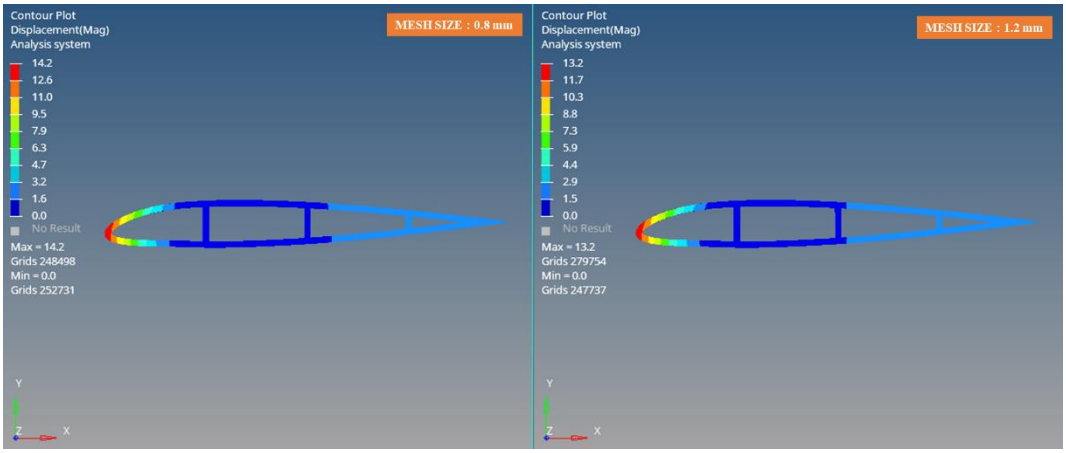

Figure 6.1. Deformation of Unit Load Model - LC Up 1

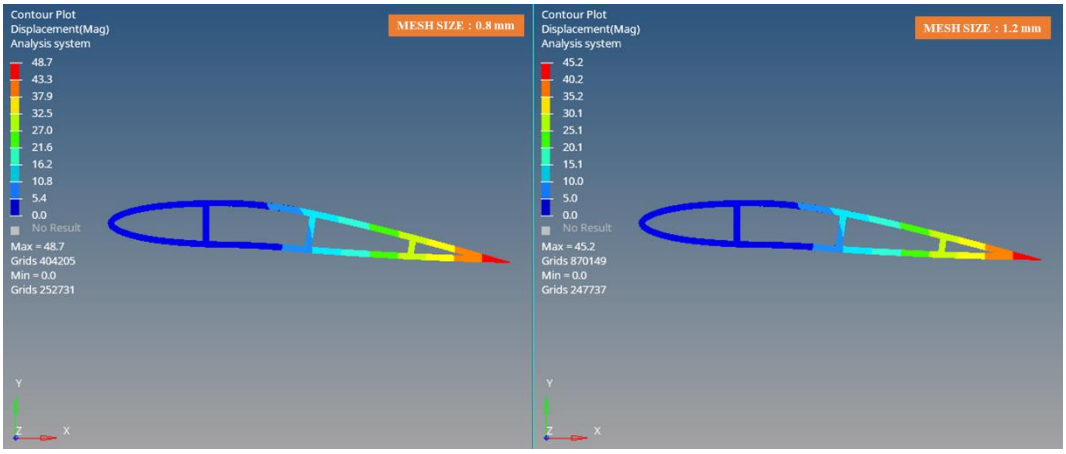

Figure 6.2. Deformation of Unit Load Model - LC Up 2

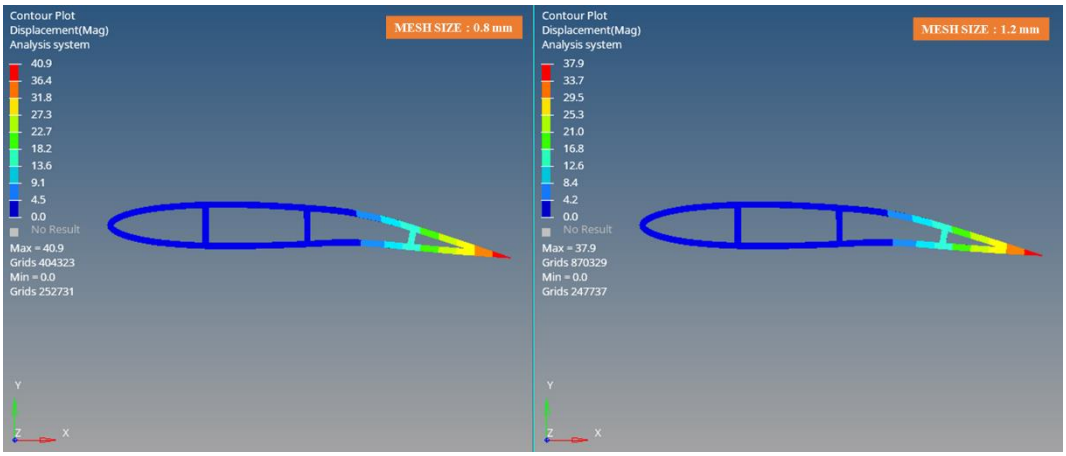

Figure 6.3. Deformation of Unit Load Model - LC Up 3

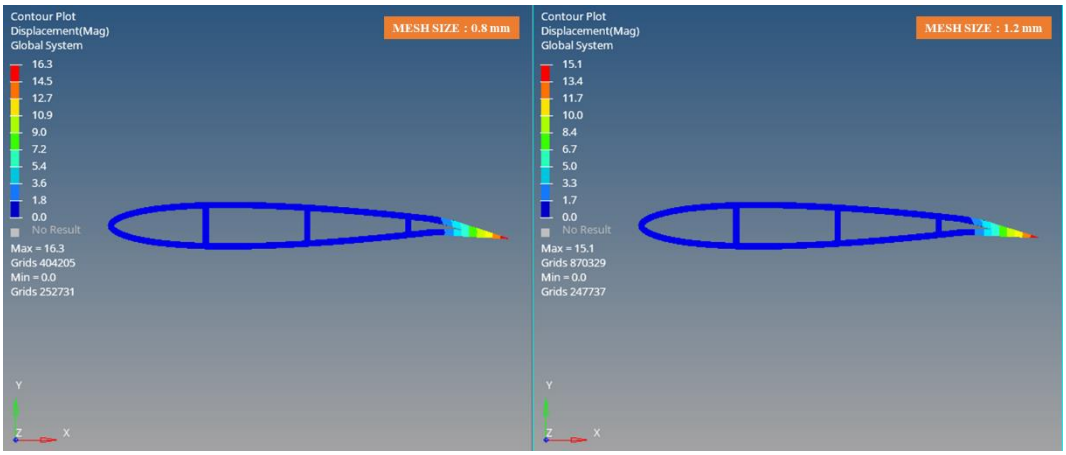

Figure 6.4. Deformation of Unit Load Model - LC Up 4

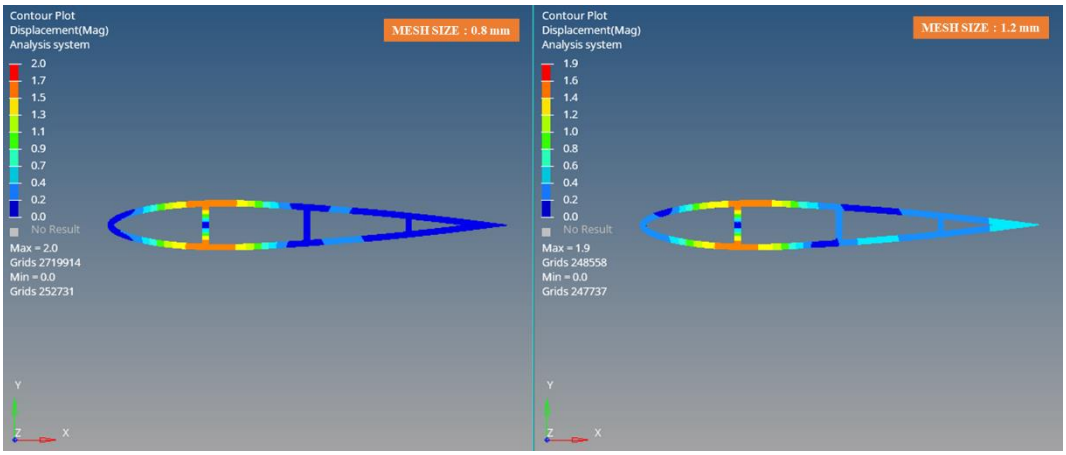

Figure 6.5. Deformation of Unit Load Model - LC Mid 1

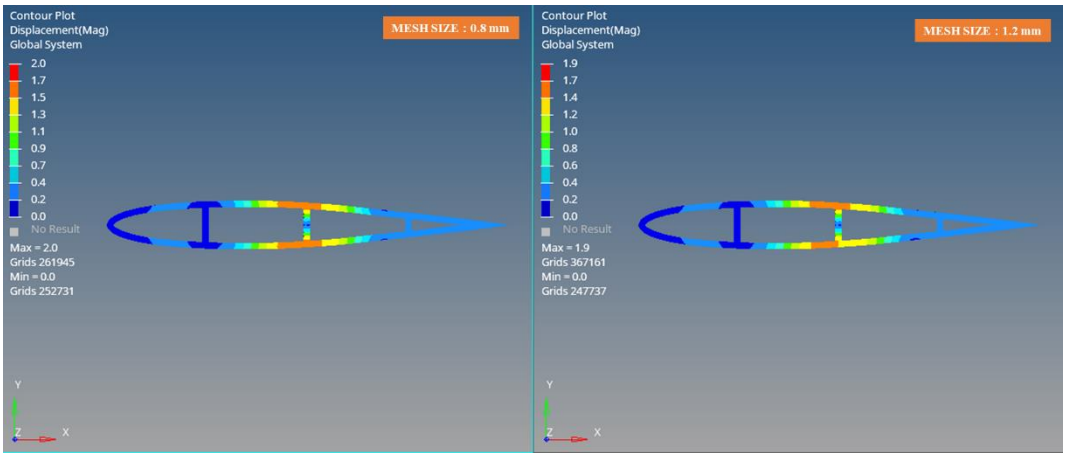

Figure 6.6. Deformation of Unit Load Model - LC Mid 2

APPENDIX B

Convergence study for Non-Linear Analysis

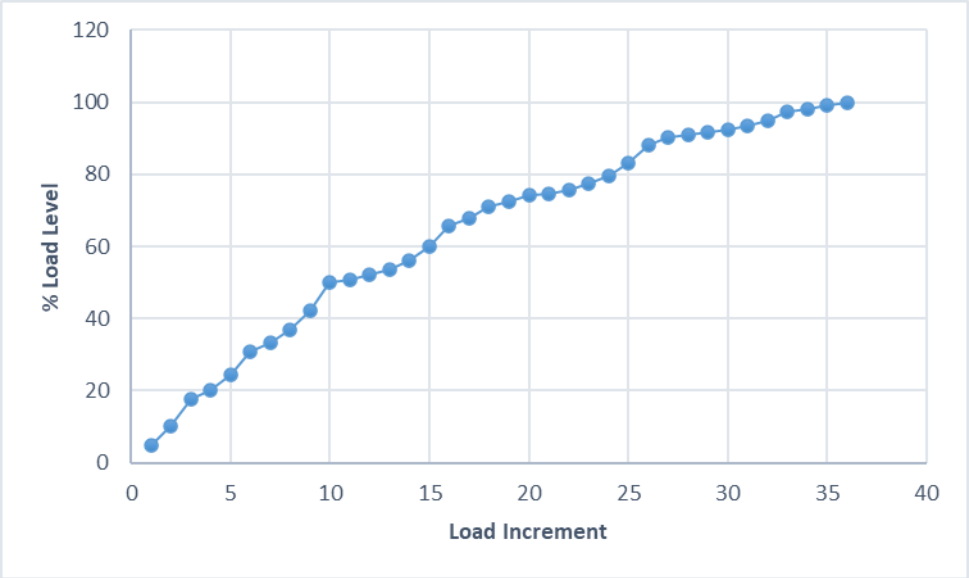

Figure 6.7. Load Level vs Load Increment Graph

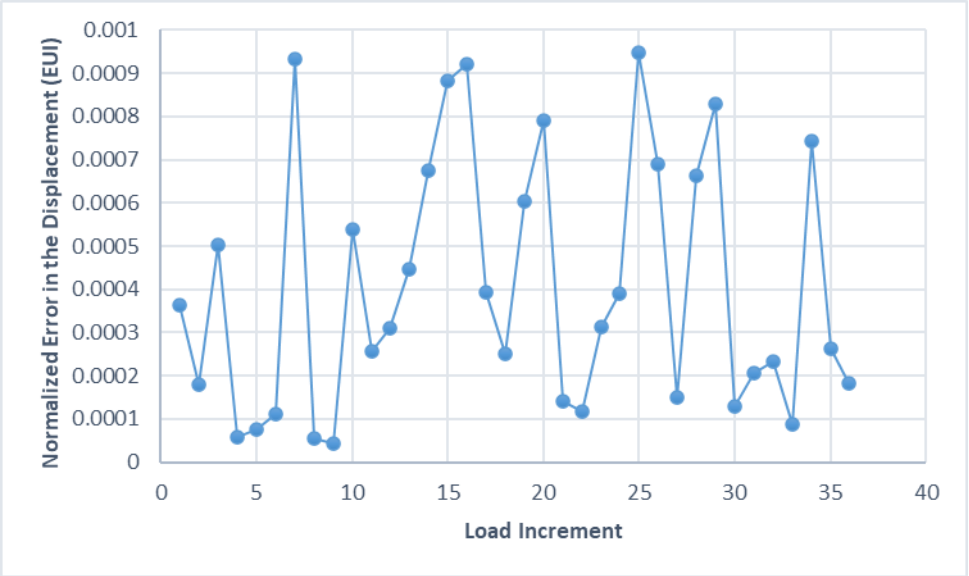

Figure 6.8. Displacement Error vs Load Increment Graph

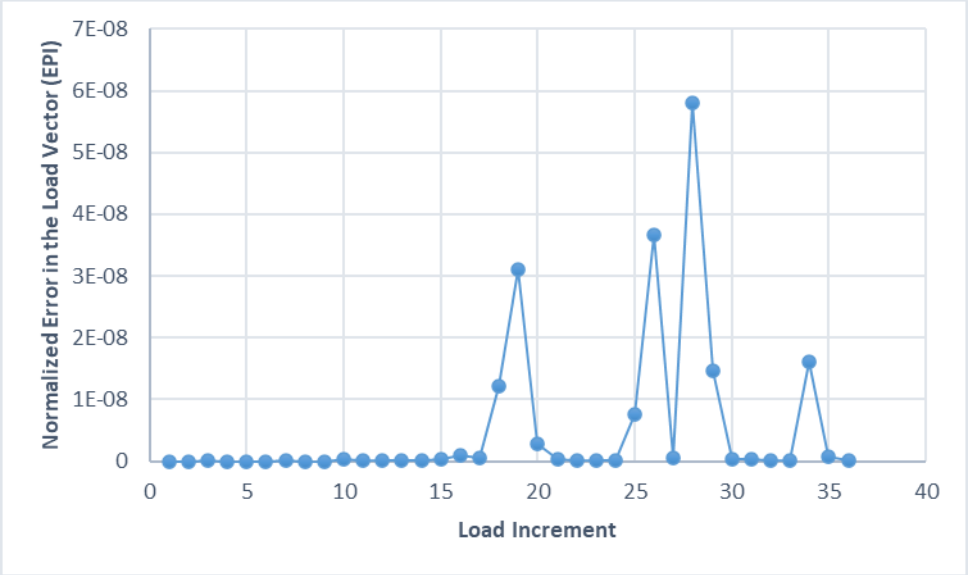

Figure 6.9. Load Vector vs Load Increment Graph

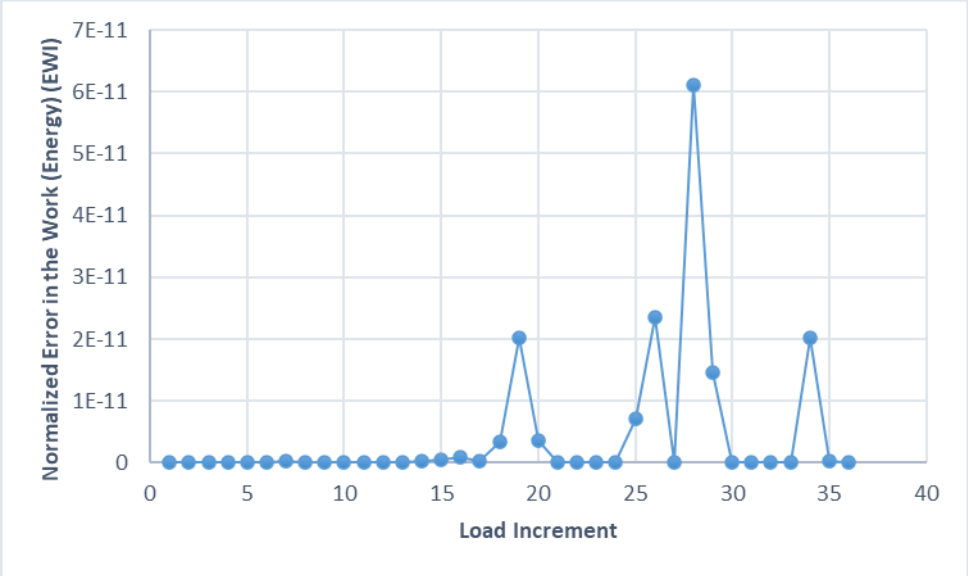

Figure 6.10. Energy Error vs Load Increment Graph